Simultaneous Rheoelectric Measurements of Strongly Conductive Complex Fluids

Ahmed Helal,[1,*] Thibaut Divoux,[2,3] and Gareth H. McKinley[1]

[1]*Massachusetts Institute of Technology, 77 Massachusetts Avenue, Cambridge, Massachusetts 02139, USA*
[2]*Centre de Recherche Paul Pascal, CNRS UPR 8641, 115 avenue Schweitzer, 33600 Pessac, France*
[3]*MultiScale Material Science for Energy and Environment, MIT-CNRS Joint Laboratory at Massachusetts Institute of Technology, Cambridge, Massachusetts 02139, USA*

(Received 31 March 2016; revised manuscript received 28 July 2016; published 9 December 2016)

We introduce an modular fixture designed for stress-controlled rheometers to perform simultaneous rheological and electrical measurements on strongly conductive complex fluids under shear. By means of a nontoxic liquid metal at room temperature, the electrical connection to the rotating shaft is completed with minimal additional mechanical friction, allowing for simultaneous stress measurements at values as low as 1 Pa. Motivated by applications such as flow batteries, we use the capabilities of this design to perform an extensive set of rheoelectric experiments on gels formulated from attractive carbon-black particles, at concentrations ranging from 4 to 15 wt %. First, experiments on gels at rest prepared with different shear histories show a robust power-law scaling between the elastic modulus G_0' and the conductivity σ_0 of the gels—i.e., $G_0' \sim \sigma_0^{\alpha}$, with $\alpha = 1.65 \pm 0.04$, regardless of the gel concentration. Second, we report conductivity measurements performed simultaneously with creep experiments. Changes in conductivity in the early stage of the experiments, also known as the Andrade-creep regime, reveal for the first time that plastic events take place in the bulk, while the shear rate $\dot{\gamma}$ decreases as a weak power law of time. The subsequent evolution of the conductivity and the shear rate allows us to propose a local yielding scenario that is in agreement with previous velocimetry measurements. Finally, to establish a set of benchmark data, we determine the constitutive rheological and electrical behavior of carbon-black gels. Corrections first introduced for mechanical measurements regarding shear inhomogeneity and wall slip are carefully extended to electrical measurements to accurately distinguish between bulk and surface contributions to the conductivity. As an illustrative example, we examine the constitutive rheoelectric properties of five different grades of carbon-black gels and we demonstrate the relevance of this rheoelectric apparatus as a versatile characterization tool for strongly conductive complex fluids and their applications.

DOI: 10.1103/PhysRevApplied.6.064004

I. INTRODUCTION

From wormlike micellar fluids to colloidal glasses, complex fluids encompass a wide array of soft materials that all display a deformable and reconfigurable microstructure, which gives rise to intermediate mechanical properties between that of liquids and solids [1–3]. Under shear, the microstructure can rearrange and interact with the flow, which may, in turn, feed back on the flow itself, triggering instabilities [4].

As such, complex fluids can exhibit a host of nonlinear effects such as shear-banding instabilities [5,6], as well as shear localization [7], wall slip [8–11], macroscopic fractures [12,13], shear-induced structuration [14–18], etc. The use of complementary local measurements such as x-ray scattering [19] and neutron spectroscopy [20] to extract, on the one hand, structural information or, on the other hand, magnetic resonance imaging [21,22], particle tracking [23], dynamic light scattering, and ultrasound imaging [24,25] to extract velocity profiles has provided valuable insights about complex fluid rheology through time-resolved measurements of the microstructure evolution under shear.

Another microstructural probe, less frequently employed, is a measurement of the electrical properties of the fluid (e.g., conductivity σ, permittivity ϵ), which, coupled with standard rheological measurements, also provides additional information on the evolution of the fluid microstructure under flow [26–32]. Previous rheoelectric studies have focused mostly on dielectric complex fluids such as polymeric materials [33–35], liquid crystals [28], colloidal suspensions [32], and electrorheological fluids [36], as well as weakly conductive materials ($\sigma \ll 1$ mS/cm) such as carbon-nanotube nanocomposites [29,30,37–41] and weakly conductive carbon-black gels [26,27,42–45].

Typical commercial rheoelectric platforms involve the use of a rheometer coupled with an electrical measuring system such as an inductance-capacitance-resistance meter that measures electric or dielectric constants simultaneously. In some studies, electrical measurements are performed using alternating current (ac) to extract the complex

*ahelal@mit.edu

permittivity of the material [27,28,42,43], while other studies have focused on the use of direct-current (dc) measurements to characterize the conductivity of weakly conductive materials under flow [26,29,30,38,40].

However, rheoelectric studies of complex fluids are rare, as they typically require the use of less common and expensive strain-controlled rheometers in which the rotary-drive and stationary torque sensors are separate. Furthermore, most previous studies have assumed homogeneous flows and have neglected the nonlinear kinematic phenomena discussed above—such as slip and shear banding—that regularly occur in conductive complex fluids [46,47] and can lead to a misinterpretation of rheological data [43–45].

Characterizing the electrical properties of strongly conductive complex fluids ($\sigma \gg 1$ mS/cm) under flow is of practical relevance for numerous applications, among which the large-scale manufacturing of conductive nanocomposites [29,30,40,48] and the design of semisolid flow-battery electrodes [44,49–51] are particularly noteworthy. For instance, the use of an embedded dispersed nanoconductor (such as carbon black) as an additive in semisolid flow cells has been shown to increase the electrochemical activity throughout the volume of the cell, leading to higher-rate performance and higher energy densities at a lower cost [44,49,52]. As such, characterizing the evolution of the conductivity of battery slurries under imposed shear is crucial for optimizing the design and operation of semisolid flow cells [53].

In this work, we use a custom-made rheoelectric apparatus to investigate the effect of shear on the conductivity of strongly conductive complex fluids. The goal of this paper is twofold. First, in Sec. II, we describe this rheoelectric test fixture, developed for stress-controlled rheometers, that is characterized by a low mechanical friction, continuous electrical contact under rotation, and low contact resistance. Second, in Sec. III, we aim at illustrating the relevance of this apparatus on a class of strongly conductive complex fluids, namely, carbon-black gels. In Sec. III A, we measure simultaneously the electrical and mechanical properties of carbon-black gels at rest, which leads to a generic power-law scaling between the elastic modulus and the conductivity of the gels. We then tackle the stress-induced yielding scenario of these gels in Sec. III B, revealing the existence of bulk rearrangements associated with minute macroscopic strains during the primary-creep regime. Finally, Sec. III C is devoted to steady-state flow and to the accurate determination of the electrical and mechanical constitutive behavior of carbon-black gels. We show that the corrections first introduced for mechanical measurements extend to electrical measurements and enable accurate conductivity measurements under shear. Section IV serves as a discussion and includes a comparison of the rheoelectric properties of carbon-black (CB) gels formulated from different grades of carbon black. This comparison illustrates how the structure of CB particles greatly affects the rheoelectric properties of the resulting gels, and it serves as a guideline for applications requiring complex fluids with high conductivities.

II. RHEOELECTRIC TEST FIXTURE

A. Description of the test fixture

Rheoelectric platforms typically involve coupling an electrical measuring system to a conventional torsional rheometer that is used to measure the rheological properties of the materials under investigation. In previous work, a number of different two-electrode geometries have been used, including cylindrical Couette [26,27,31], plate-plate [28,39,43,45], and ring geometries [29,30,37,38] as well as pipe flow [32]. The difficulty inherent in performing simultaneous rheoelectric measurements lies in the additional friction caused by the electrical connection to the rotating electrode (typically through a slip ring), which can induce large errors in the measurement of the torque when measured at the same electrode. Controlled-rate rheometers are, therefore, generally preferred for this class of measurements as they allow the user to measure torque on the stationary electrode, thus decoupling the electrical and rheological measurements. However, rate-controlled rheometers are more expensive and less common than stress-controlled rheometers and are less well suited for measuring yielding transitions that are common in highly filled conductive materials. These limitations motivate the development of an alternative apparatus.

A schematic of the experimental test fixture, later referred to as the rheoelectric test fixture and used to perform the simultaneous rheoelectric measurements, is shown in Fig. 1. The apparatus is built around two parallel plates (of radius $R = 20$ mm and surface roughness $R_a = 0.1$ μm, as determined by a Mitutoyo surface profilometer) that form a two-electrode cell separated by a distance H with the conductive sample sandwiched between them. The upper rotating plate is connected to a stress-controlled torsional rheometer (TA Instruments, AR-G2) that applies a torque and measures the resulting shear strain. The plate-plate geometry is chosen here as it allows for a homogeneous electric field and can be used to correct for wall-slip effects through measurements at multiple gap settings [54]. However, the shear rate $\dot{\gamma}$ is not homogeneous in the parallel-plate geometry and depends on the radial position r, as follows: $\dot{\gamma}(r) = r\Omega_{\mathrm{rot}}/H$, where Ω_{rot} denotes the angular velocity of the upper plate. The impact of such inhomogeneity on the rheological measurements is taken into account and is discussed in Sec. III C. The geometry forms a closed electrical circuit that incorporates (i) the conductive sample, (ii) the plates, (iii) the electrical measuring system formed by a potentiostat (Solartron SI1287) with an impedance analyzer (SI1266), and (iv) a solvent trap (constructed from

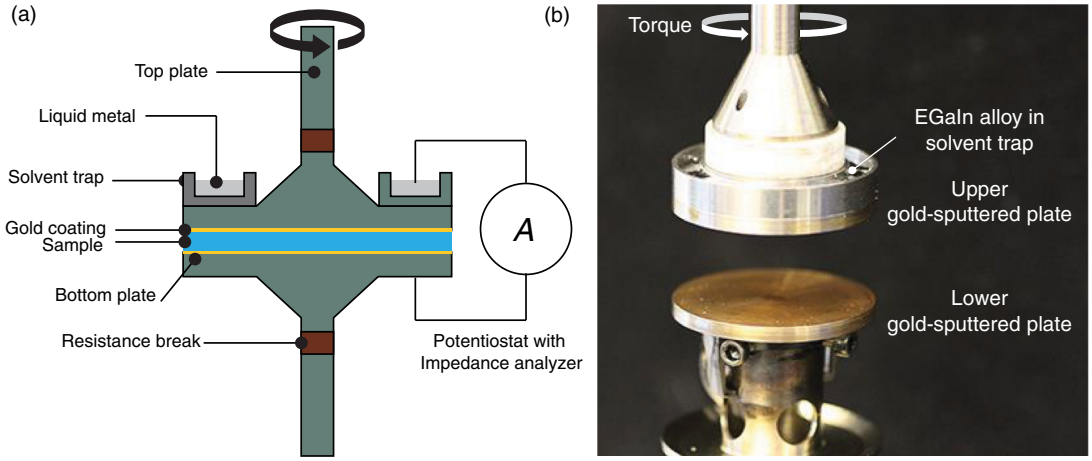

FIG. 1. (a) Schematic of the rheoelectric test fixture. The sample is sandwiched between two parallel plates ($R = 20$ mm) that form a two-electrode closed electrical circuit. The rotating upper plate is driven by a stress-controlled rheometer that applies stress and measures strain. Liquid metal (EGaIn) in the solvent trap provides a low-friction electrical contact to the rotating shaft. The plates are sputter coated in gold to reduce contact resistance. (b) Photograph of the rheoelectric fixture.

a machined annulus of SS316) filled with eutectic gallium-indium liquid metal (EGaIn, from GalliumSource). EGaIn is a liquid metal at room temperature which provides a safe nonhazardous alternative to other liquid metals such as mercury [34] and is used to create a low-friction continuous electrical connection to the rotating shaft. Finally, to reduce the contact resistance, the plates are sputter coated with gold using a Pelco SC-7 sputterer for 10 min. Unless otherwise noted, all rheoelectric tests are performed at a temperature $T = (23.0 \pm 0.3)$ °C, with a gap $H = 750$ μm.

Under static conditions, two types of electrical conductivity measurements are of interest: dc and ac tests. In a dc test, a constant potential $\phi_0 = 100$ mV is applied and the corresponding current I is measured. The apparent dc conductivity σ_a is then given by

$$\sigma_a = \frac{H}{\pi R^2}\frac{I}{\phi_0}, \tag{1}$$

where H is the sample gap imposed by the rheometer. In an ac test, a sinusoidal potential $\phi = \phi_0 \sin(\omega t)$ is applied and the corresponding alternating current is measured. The complex impedance is defined as

$$Z^*(\omega) = \frac{\phi}{I} = Z' - iZ'', \tag{2}$$

where Z' and Z'' are, respectively, the real and imaginary contributions to the impedance. Note that Z' and Z'' are the electrical analog of the real and imaginary contributions (η' and η'', respectively) to the complex viscosity $\eta^*(\omega)$ in rheology, which will be of interest in Sec. III [55,56]. Finally, the complex impedance is related to the complex dielectric permittivity through the following expression [57]:

$$\epsilon^* = \frac{H}{Z^* i\omega\epsilon_0\pi R^2}. \tag{3}$$

In both ac and dc measurements, it is important to note that the measured resistances and impedances correspond to a sum of two contributions: a bulk resistance resulting from the sample resistance, and an interfacial contact resistance representing how readily the electrons can flow through the interface between the sample and the plates so that

$$\mathcal{R}_{\text{measured}} \equiv \frac{\phi_0}{I} = \mathcal{R}_{\text{contact}} + \frac{H}{\sigma_{\text{bulk}}\pi R^2}. \tag{4}$$

Traditionally, by conducting measurements at different gaps, the contribution of the contact resistance can be calculated in conjunction with Eq. (4) and corrected for [57]. For strongly conductive fluids, the relative contribution of the contact resistance becomes increasingly important as the bulk conductivity increases and cannot be neglected if accurate measurements are desired. Unless stated otherwise, the conductivity and impedance discussed hereafter correspond to the apparent quantity defined, respectively, in Eqs. (1) and (2).

B. Mechanical and electrical calibration

We first discuss the mechanical calibration of the rheoelectric test fixture and justify the preferential use of liquid metal in the electrical circuit compared to two other techniques, namely, a gold spring and a salt solution, which are commonly used in other existing rheoelectric configurations. On stress-controlled rheometers, friction acting on the rotating shaft during electrical measurements under shear can impede simultaneous rheological measurements. To quantify such friction, we perform measurements of the torque $\mathcal{M}$ associated with the friction inherent to different electrical couplings: EGaIn, a gold-leaf spring,

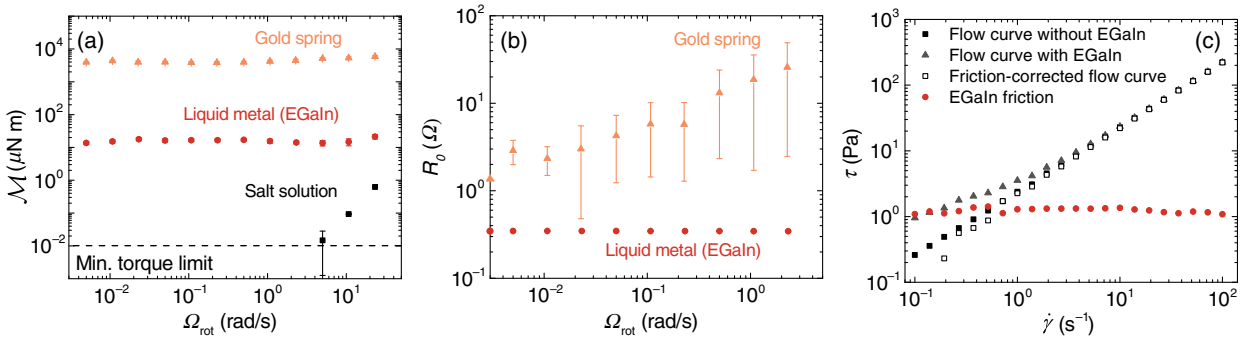

FIG. 2. (a) Total measured torque $\mathcal{M}$ resulting from the friction of the electrical connection to the rotating shaft as a function of the angular velocity Ω_{rot} of the upper plate. Measurements are conducted in the absence of a sample and for different electrical contacts: a gold-leaf spring, liquid metal (EGaIn), and a salt solution. (Inset) Temporal fluctuations of the frictional torque $\mathcal{M}$ from the EGaIn alloy are represented by the error bar shown for each angular velocity and can, in general, be neglected. (b) Setup dc resistance $\mathcal{R}_0$ measured in the absence of a sample as a function of Ω_{rot} for two electrical conductors: either a gold-leaf spring or a liquid metal (EGaIn). Error bars are determined by calculating the standard deviation of the temporal signal over 180 s. The use of a salt solution as a conductor does not allow for dc measurements, as the ionic species will polarize only under dc. (c) Measured flow curves showing shear stress τ vs shear rate $\dot{\gamma}$ for a Newtonian calibration oil and illustrating the friction correction resulting from EGaIn. The red filled circles represent the friction calibration performed with EGaIn in the absence of a sample prior to the flow curve measurement. The green triangles and black squares represent, respectively, the flow curves measured with and without the liquid metal. The open black squares represent the final corrected flow curve.

and a salt solution. Results are reported as a function of the angular velocity Ω_{rot} of the upper plate in Fig. 2(a). The friction due to the liquid metal lies 2 orders of magnitude below that of the gold spring and is constant over four decades of angular velocity, thus leading to a straightforward correction for mechanical friction. This constant friction arises primarily from the thin oxide layer that forms on top of the liquid metal when in contact with air [58,59]. Furthermore, the temporal fluctuations of the friction contribution to the stress can, in general, be neglected during simultaneous measurements when operating at stresses larger than the background friction level shown by the error bars in Fig. 2(a). At $\Omega_{rot} = 1$ rad/s, the friction torque of the EGaIn test fixture is $\mathcal{M} = 12.9 \pm 2.9$ μN m.

Regarding the electrical calibration, the dc resistance $\mathcal{R}_0$ of the test fixture in the absence of any sample is measured as a function of the angular velocity Ω_{rot} for a closed electrical circuit using either EGaIn or a gold spring [Fig. 2(b)]. The liquid metal leads to a low resistance, $\mathcal{R}_0 = 0.3$ Ω, that is independent of angular velocity, which makes the contribution to the electrical resistance from the test cell easy to take into account. On the contrary, the configuration involving the gold-leaf spring shows a larger and much noisier resistance that increases with the plate rotation speed. We also emphasize that the use of a salt

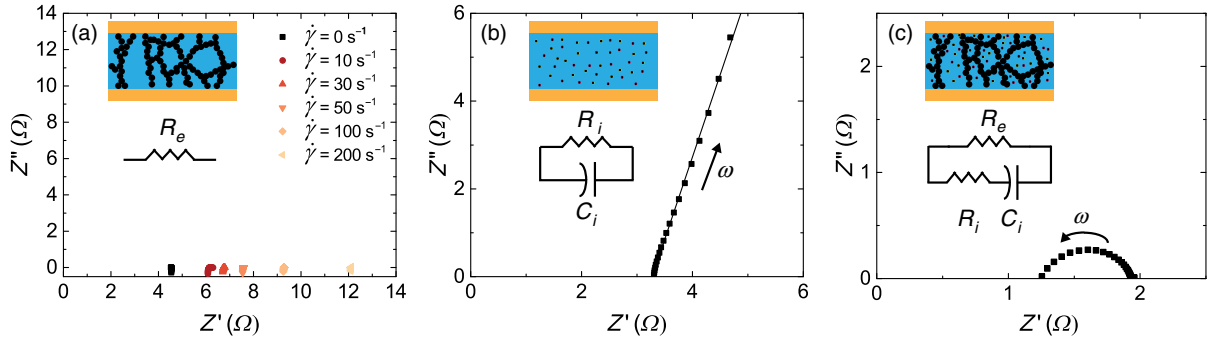

FIG. 3. Nyquist plots of complex impedance for three different classes of conductive complex fluids and their corresponding equivalent circuits. (a) Electronic conductor: suspension of attractive soot particles (carbon black, VXC72R) dispersed in mineral oil at 8 wt %. The conductivity is measured at different shear rates coded in color: $\dot{\gamma} = 0$, 10, 30, 50, 100, and 200 s^{-1} from dark to light color. (b) Ionic conductor (Oakton 2764 μS/cm KCl solution) measured under static conditions for $H = 750$ μm. The linear fit corresponds to the model blocking circuit shown in the inset. (c) Mixed conductor: lithium polysulfide suspension containing 2.5M Li_2S_8, 0.5M LiTFSI, and 1M $LiNO_3$, with 1.5-vol % Ketjenblack carbon measured under static conditions. We perform ac tests for $10^2 \leq \omega \leq 10^4$ Hz.

solution only allows for ac measurements at low potentials ($\phi_0 \leq 10$ V) and tends to have a complex electrical signature due to ion mobility, which can complicate the electrical corrections [57].

From both a mechanical and an electrical standpoint, the test configuration using EGaIn is the most suitable for rheoelectric measurements on stress-controlled rheometers. As a result of the low friction, we are able to perform simultaneous measurements of rheology and conductivity, an example of which is shown in Fig. 2(c) on a calibration oil (N1000, Cannon Instrument Company). The additional friction resulting from the EGaIn is constant at about 1.2 Pa. By subtracting the latter value from the flow curve measured using the same experimental fixture, one recovers, with high accuracy, the true flow curve of the calibration oil measured in the absence of the electrical connections, at least for shear stresses $\tau \geq 1.2$ Pa. For shear stresses $\tau < 1.2$ Pa, the corrected data departs appreciably from the constitutive equation, showing that, although conductivity measurements may still be performed, stress measurements should be conducted separately in this low stress range, i.e., without the upper electrode immersed in the liquid metal (EGaIn).

C. Benchmark electrical measurements

To illustrate the ability of the EGaIn rheoelectric fixture to perform accurate conductivity measurements, we conduct a series of benchmark ac measurements ($\phi_0 = 100$ mV, $10^2 \leq \omega \leq 10^4$ Hz) on different classes of conductive complex fluids, namely, electronic, ionic, and mixed conductors. The ac response of these fluids are reported in Fig. 3, where the imaginary part Z'' of the complex impedance is plotted vs the real part Z' of the complex impedance. Such a representation, also known as a Nyquist plot [57], is analogous to a Cole-Cole plot for rheological measurements.

First, we report the response of an electronic conductor, here a suspension of attractive soot particles (carbon-black VXC72R, Cabot) dispersed in mineral oil at 8 wt % that is measured under steady simple shear flow. The electrical resistance of this suspension is well represented by a pure Ohmic resistor and corresponds to a series of points that sit on the horizontal axis of the Nyquist plot [Fig. 3(a)]. As the shear rate is increased, the resistance increases approximately threefold due to the disruption of the floculated carbon-black network under shear.

Second, we report an example of an ionic conductor (Oakton 2764 μS/cm KCl solution, Cole-Parmer) measured under static conditions for $H = 750$ μm and at $T = 25.0$ °C [Fig. 3(b)]. This suspension is represented by an Ohmic resistor in parallel with an imperfect capacitor $[Z^*(\omega) = \mathcal{R}_i + 1/(i\omega C_i)^\alpha]$, represented by a constant phase element of phase α. In the Nyquist plot, it appears as a line of slope $\tan(\alpha\pi/2)$ that intercepts with the horizontal axis at $Z' = \mathcal{R}_i$, which represents the ionic resistance of the solution. The experimental data are indeed well described by a blocking circuit [the black line in Fig. 3(b)]. Supplemental measurements at various gaps and Eq. (4) allow us to correct for the contact resistance and thus infer the bulk conductivity of the ionic solution [Fig. 4(a)]. The contact resistance and bulk conductivity are found to be, respectively, $\mathcal{R}_c = 0.94$ Ω and $\sigma_b = (2.76 \pm 0.01)$ mS/cm at $T = 25.0$ °C [Fig. 4(b)], in excellent agreement with the value provided by the manufacturer ($\sigma = 2.764$ mS/cm).

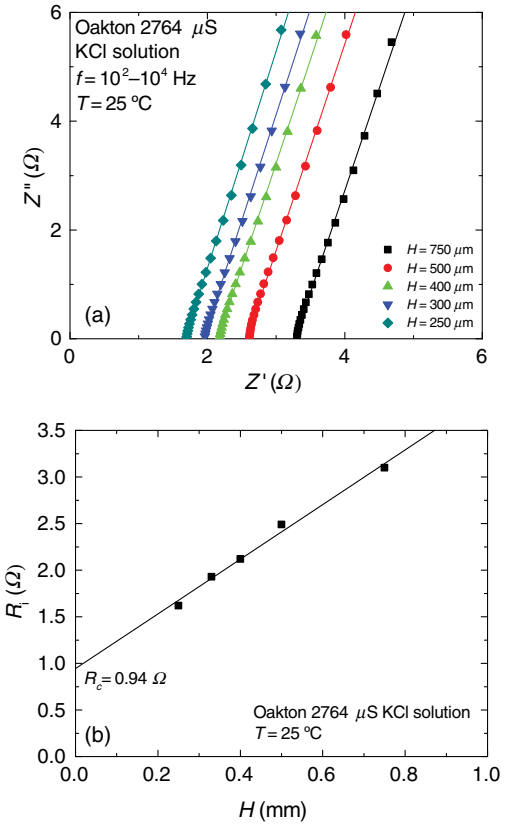

FIG. 4. (a) Nyquist plot of the complex impedance for an ionic conductor (Oakton 2764 μS/cm KCl solution) measured under static conditions for various gap heights, $H = 750$, 500, 400, 330, and 250 μm. This suspension is characterized by an Ohmic resistor in parallel with an imperfect capacitor $[Z^*(\omega) = \mathcal{R}_i + 1/(i\omega C_i)^\alpha]$, represented by a constant phase element of phase α and appearing in the Nyquist plot as a line of slope $\tan(\alpha\pi/2)$ that intercepts with the horizontal axis at $Z' = \mathcal{R}_i$. The colored lines correspond to the best linear fit of the data for each gap setting. (b) Ionic resistance $\mathcal{R}_i$ as determined in (a) vs the gap height H. The present data set shows that the sample resistance is divided into two contributions: a contact resistance $\mathcal{R}_c$ which corresponds to the intercept and a bulk resistance associated with the slope [see Eq. (4)]. The black line is the best linear fit of the data and leads to $\mathcal{R}_c = 0.94$ Ω and $\sigma_b = (2.76 \pm 0.01)$ mS/cm.

Finally, we consider a third sample, which is an example of a semisolid battery material that consists of a mixed conductor (a lithium polysulfide suspension containing $2.5M$ Li_2S_8, $0.5M$ LiTFSI, and $1M$ $LiNO_3$, with

1.5-vol % Ketjenblack EC600JD carbon black). Its equivalent circuit, which is the mechanical analog of the Jeffreys model in rheology [60], corresponds to a depressed semicircle that intersects the horizontal axis at $Z' = \mathcal{R}_e\mathcal{R}_i/(\mathcal{R}_e + \mathcal{R}_i)$ and $Z' = \mathcal{R}_e$, respectively. The Nyquist plot of this slurry, determined under static conditions using the rheoelectric fixture, is shown in Fig. 3(c). The ionic and electronic conductivities are estimated to be $\sigma_i = 2.6$ mS/cm and $\sigma_e = 3.7$ mS/cm, respectively, in agreement with measurements previously reported on the same material [49].

To conclude, the use of gold-sputtered plates and EGaIn to close the electrical circuit allow for accurate electrical measurements on a wide variety of strongly conductive complex fluids, which demonstrate the versatility of the EGaIn rheoelectric test fixture. In the rest of the paper, we employ the rheoelectric fixture to investigate, in detail, one of the aforementioned model systems, namely, carbon-black gels.

III. RHEOELECTRIC STUDY OF CARBON-BLACK GELS

We focus on carbon-black dispersions as a case study of a strongly conductive complex fluid to illustrate the additional insight that can be gained from this rheoelectric apparatus. Carbon black (CB), which refers generically to colloidal soot particles produced from the incomplete combustion of fossil fuels, is utilized extensively in a wide variety of industrial applications, including batteries, paints, and coatings as well as filled rubbers and tires. CB serves as an additive to convey protection from ultraviolet light, increase toughness, and improve processability, and to enhance electrical conductivity [61,62]. Composed of permanently fused "primary" particles whose diameter is about 30 nm [63], CB particles are of typical size, 200–500 nm, and display short-range attractive interactions of typical strength 30 k_BT [64].

When dispersed in a liquid hydrocarbon, carbon-black particles form a space-spanning network, even at small volume fractions (typically 1% to 5%) [65,66]. The resulting gels are reversible, as they are destroyed by large shear and reform once the flow is stopped. The elastic modulus and yield stress depend on the flow history, which can be used to tune the solidlike properties of the gel at rest [16,67].

Finally, shear-induced changes in microstructure are known to strongly affect the electrical properties of carbon-black gels as the percolated network ruptures under shear [26,31,48]. Depending on the choice of carbon black, the conductivity of the gel either decreases by several orders of magnitude as the material is sheared and undergoes a conductor-to-insulator transition [31], or, in the case of more-conductive samples, the conductivity only decreases by a small factor under shear [26].

In this work, a number of CB dispersions are prepared in the absence of any additional dispersant by mixing CB particles of different grades [VXC72R, Monarch 120 and Elftex 8 from Cabot chemicals (Billerica, Massachusetts), and Ketjenblack EC600 from Akzo Nobel (USA)] into a light mineral oil (Sigma, density 0.838 g/cm^3, viscosity 20 mPa s), as described in Ref. [46] at weight concentrations c ranging from 4 to 15 wt %. The samples are sonicated for 4 h and are mixed thoroughly prior to any use.

In the following sections, we mainly report data obtained with an 8-wt % carbon-black gel (VXC72R), which have been extensively studied in the literature [16,18,47,68]. Such a gel is used here as a model conductive complex fluid, as it shows neither chemical aging nor any evaporation, and it allows for reproducible measurements over long durations. Furthermore, the VXC72R carbon black has been specifically developed for high-conductivity applications and is an ideal system for exploring the rheoelectric properties of strongly conductive complex fluids. Using the rheoelectric test fixture characterized in Sec. II, we first determine the electrical and mechanical solidlike properties of the CB gel at rest, which is brought to rest through different flow-cessation protocols (Sec. III A). We then focus on transient flows and perform creep experiments to study the yielding behavior of the CB gel from an electrical perspective (Sec. III B).

Finally, we report an extensive study of steady shear flows of the CB gel and show how electrical measurements allow us to detect flow heterogeneities and wall slip (Sec. III C). To conclude, a discussion section including a quantitative comparison of the rheoelectric properties of CB gels, prepared with different grades of CB, shows how the nature of the CB particles greatly affects the ensuing rheoelectric properties of the gels. Such analysis, made possible with the rheoelectric fixture introduced here, is key for numerous applications where the selection of an appropriate conductive sample should obey specific design constraints on both the mechanical and electrical properties (Sec. IV).

A. Tuning rheoelectric properties of carbon-black gels using shear history

Recent studies have shown that the mechanical properties of weak attractive gels can be tuned by controlling their shear history [62,67,69]: abrupt flow cessation or "quenching" leads to highly elastic gels, whereas slow cessation of shear leads to weak solids characterized by a vanishingly small yield stress for a decreasing flow-cessation rate.

In this subsection, we investigate the evolution of the electrical properties concomitantly to the elastic properties of the gel prepared by flow-cessation experiments at various cessation rates. Ramps of decreasing stress ranging from $\tau = 100$ Pa to $\tau = 0$ Pa and bringing the sample to complete rest are performed in $N = 100$ successive steps. The upper stress value is applied for 5 min before the start

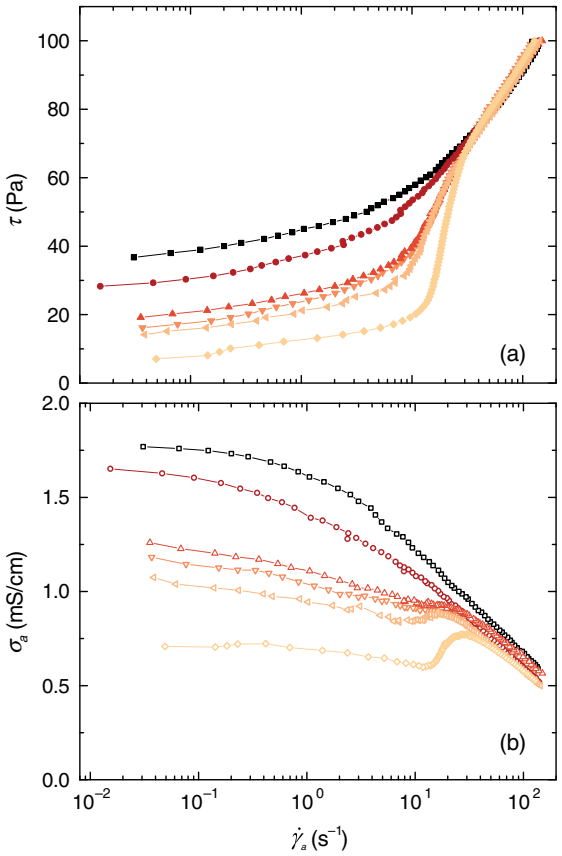

FIG. 5. (a) Stress τ vs apparent shear rate $\dot{\gamma}_a$. (b) Apparent conductivity σ_a vs the apparent shear rate $\dot{\gamma}_a$ measured in an 8-wt % VXC72R carbon-black gel during decreasing ramps of stress ranging from $\tau = 100$ Pa to $\tau = 0$ Pa. Every test is performed in $N = 100$ steps of 1 Pa each, and a different duration per point Δt is used for each experiment. From top to bottom, the values of Δt are 1, 6, 15, 21, 30, and 120 s.

of each decreasing ramp, and it is chosen to be large enough to ensure that the sample is fully fluidized and that any previous flow history is erased. The flow-cessation rate is controlled through the duration of each step Δt, that is varied in each test from 1 to 120 s. The resulting flow and conductivity curves are plotted in Fig. 5.

As the stress is ramped down, the shear rate decreases and the conductivity concomitantly increases. Such results coincide with the fact that the gel transitions from a fully fluidized state at high shear rates to a solidlike state at rest. The gel structure builds up, forming a percolated network which accounts for the solidlike behavior and the conductivity increase. For $\dot{\gamma}_a > 30$ s^{-1}, the flow and conductivity curves obtained at different cessation rates collapse, indicating that, in this region, the gel is fully fluidized and not sensitive to the flow history.

At lower shear rates, the flow and conductivity curves both become strongly sensitive to the flow-cessation rate: slower ramps (or increasing shear durations Δt spent at each rate) lead to lower yield stress (defined as the stress extrapolation for vanishing shear rates) and lower apparent conductivity. These results are associated with the growth of a solidlike structure as the gel, whose formation kinetics are strongly affected by Δt, comes to a stop.

To characterize the final state of the gel once the stress ramp is over, we record both the terminal value of the conductivity σ_0 and the linear elastic moduli G_0' determined by oscillations of small amplitude ($\gamma = 0.2\%$) at $f = 1$ Hz. These measurements are performed 90 min after the end of the stress ramp to ensure that mechanical and electrical equilibrium is reached [see Fig. 12 in Appendix A]. Repeating the experiment for various step durations, Δt allows us to extract a series of pairs $\{G_0', \sigma_0\}$ that are plotted in Fig. 6. The elastic modulus G_0' displays a power-law increase with the apparent conductivity at rest (σ_0), showing that there is a correlation between the mechanical and electrical properties of the gel at rest: slower ramps lead to softer and less-conductive gels, a signature of lower connectivity in the sample-spanning network of CB aggregates. The latter results hold true at lower concentrations of carbon-black particles. Data obtained following the same protocol with 4- and 6-wt % carbon-black gels (filled triangle and filled circle, respectively, in Fig. 6) show the same result and collapse on a master curve for $\sigma_0 \geq 0.1$ mS/cm, where $G_0' \propto \sigma_0^{\alpha}$, with $\alpha = 1.65 \pm 0.04$. The latter result hints at a unique gelation scenario kinetically driven by shear and not sensitive to the particle

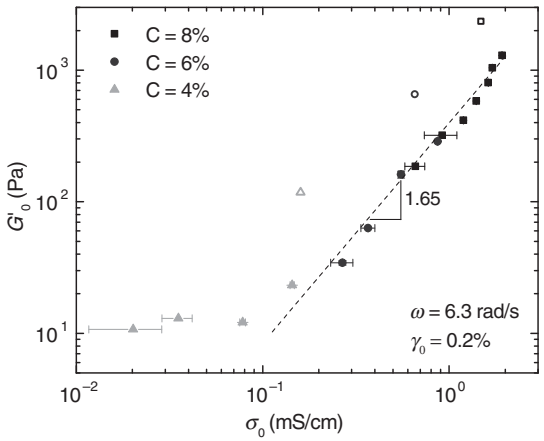

FIG. 6. Elastic modulus G_0' of carbon-black gels vs conductivity σ_0 measured at rest, 90 min after the end of a stress ramp decreasing from 100 to 0 Pa and composed of 100 steps. Each point corresponds to different step durations Δt during the ramp, from $\Delta t = 1$ s to $\Delta t = 120$ s, while symbols stand for different concentrations of carbon black (VXC72R): $c = 4$ (filled triangle), 6 (filled circle), and 8 wt % (filled square). Open symbols represent an instantaneous quench from $\tau = 100$ Pa to $\tau = 0$ Pa. Data for the 8-wt % gel corresponds to the experiment reported in Fig. 5. Oscillatory measurements are performed at a strain $\gamma_0 = 0.2\%$ and a frequency $f = 1$ Hz. The dashed line corresponds to the best power-law fit of the data for $\sigma_0 \geq 0.1$ mS/cm, i.e., $G_0' = \tilde{G}_0' \sigma_0^{\alpha}$, with $\tilde{G}_0' = 400$ Pa(cm/mS)$^{\alpha}$ and $\alpha = 1.65 \pm 0.04$.

concentration, at least for sufficiently strong gels with $G_0' \gtrsim 10$ Pa.

Finally, we have also performed sudden quenches; that is, the CB gel is brought from $\tau = 100$ Pa to $\tau = 0$ Pa, within 1 s. In that case, the conductivity is comparable to that obtained with the fastest ramp previously explored (of total duration 100 s), but the elastic modulus is much larger so that the rheoelectric properties at rest (the open symbols in Fig. 6) do not fall onto the same master curve as the ramp tests of longer duration. However, we emphasize that the terminal elastic modulus still appears to grow as a power-law function of the conductivity, and the exponent is compatible (within error bars) with the value determined for more gradual flow cessations.

For the three concentrations examined, abruptly stopping the shear flow leads to a gel of enhanced elasticity, which hints at a specific gel microstructure that is well adapted to sustain shear and yet not more conductive (and hence more percolated) than gels formed in a fast ramp of 100 s. These results are in line with the idea that the mechanical and electrical networks are not identical [70] and can be affected differently by shear. These results show that the electrical properties of carbon-black gels can be tuned through the shear history in parallel with the mechanical properties.

B. Stress-induced yielding

In this section, we turn to the transient behavior of carbon-black gels and investigate the evolution of the rheoelectric properties of the 8-wt % CB gel (VXC72R) during its stress-induced yielding transition. Prior to each creep experiment, the CB gel is presheared at $\dot{\gamma} = 200$ s^{-1} for 5 min to erase the previous flow history and left to rebuild for 20 min at $\tau = 0$ Pa. A constant stress is then applied from $t = 0$ and the resulting shear-rate response $\dot{\gamma}(t)$ and the apparent conductivity response $\sigma_a(t)$ are monitored simultaneously. Results for different applied shear stresses are reported in Fig. 13 in Appendix A.

All of the creep experiments display three characteristic regimes, which we illustrate in Fig. 7(a), for the case of an experiment conducted at $\tau = 22$ Pa. (i) First, for $t < 3800$ s, the shear rate decreases as a power law, $\dot{\gamma}(t) \sim t^{-0.9}$, while the apparent conductivity increases as a weak power law, $\sigma_a(t) \sim t^{0.035}$ (see Fig. 14 in Appendix A for a logarithmic plot of the same data). (ii) Second, for 3800 s $\leq t \leq$ 4600 s, a jump in the shear rate is observed and the apparent conductivity drops concomitantly by half and fluctuates. (iii) Third, for $t > 4600$ s, the shear rate undergoes a second steep increase, while the apparent conductivity drops, before both observables tend towards a final steady-state value. The mechanical response alone of this "delayed yielding" has previously been reported in a Couette geometry [46,47]. Coupled with time-resolved velocimetry, the latter studies have shown that the three regimes can be interpreted as a succession of (i) the homogeneous deformation above the micron scale, followed by (ii) a total wall-slip regime associated with the first rapid increase of $\dot{\gamma}(t)$, and the growth of a transient shear band [a second increase of $\dot{\gamma}(t)$] to finally reach (iii) a homogeneous flow.

The unique signature of these regimes also appears in the apparent conductivity response, which provides further insights into the yielding behavior. Indeed, in the first regime, the increase in apparent conductivity clearly demonstrates that either the bulk microstructure of the sample or the number of contacts between the sample and the wall is evolving. The latter result highlights the high sensitivity of the rheoelectric test fixture in the first regime, where the sample deformation remains extremely low [$\gamma \lesssim 4\%$ for $t < 3800$ s] and where other techniques, including ultrasonic velocimetry [47], fail to provide

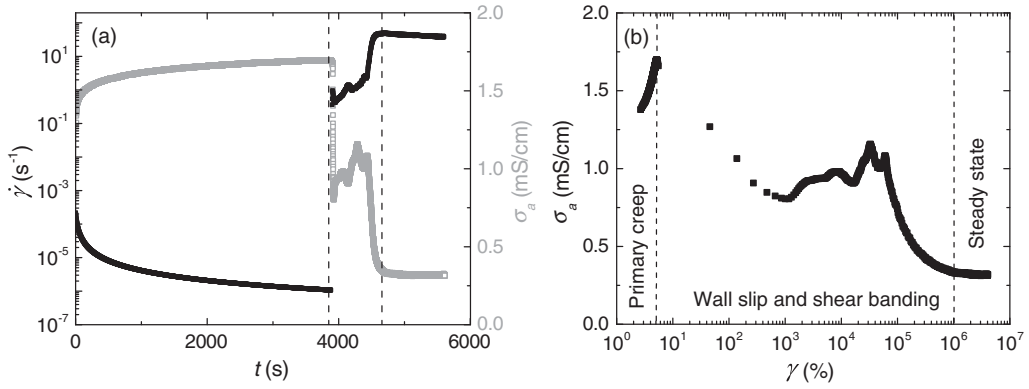

FIG. 7. Creep experiment in an 8-wt % carbon-black gel (VXC72R) at $\tau = 22$ Pa. (a) Shear-rate response $\dot{\gamma}(t)$ and apparent conductivity response $\sigma_a(t)$. The shear rate is derived numerically from the strain measured by the rheometer to increase the precision. The jump observed in the curves at $t = 3800$ s marks the onset of a total wall-slip regime followed by the growth of a transient shear band [47] before the sample reaches a homogeneous steady state. (b) Apparent conductivity σ_a vs strain γ for the same data set. In both (a) and (b), the vertical dashed line marks the three different flow regimes discussed in the text: primary creep, heterogeneous flow, and steady-state flow.

time-resolved data due to a lack of resolution. In the intermediate regime, the decrease in the apparent conductivity is compatible with the onset of slip, which is expected to increase the electrical resistance at the interface. Moreover, the oscillations observed in the apparent conductivity are strongly reminiscent of the stick-slip-like motion of the carbon-black gel reported in Ref. [47], where alternating plug and shear-flow regions have been observed. Finally, in the third regime, the conductivity reaches its lower, constant value—which is in agreement with a fully fluidized sample that makes uniform electrical contact with the wall, flowing homogeneously at steady state.

A cross plot of the apparent conductivity σ_a vs the strain γ is shown in Fig. 7(b). In this representation, the delayed yielding and the three regimes discussed above are readily observed. In the primary-creep regime, we observe a linear increase of apparent conductivity with strain, a signature of the increase of connectivity within the carbon-black network in bulk or at the interface. In the intermediate regime, wall slip and shear banding result in a sudden decrease of apparent conductivity with strain as the sample fails at the interface, increasing the contact resistance. Finally, in the third regime, the apparent conductivity reaches a constant value as the strain increases, an indication that the system is fully fluidized and has reached steady state.

Finally, to determine whether the increase of the conductivity during the primary-creep regime is associated with bulk rearrangements, or with the evolution of the sample in the vicinity of the plates, we perform supplemental creep experiments at $\tau = 30$ Pa for gaps of different heights, $H = 660$, 500, and 330 μm. The corresponding shear rate and the apparent conductivity responses are shown in Fig. 8. For the three gaps studied, the shear-rate responses display a similar evolution, indicating that the material is subjected to the same delayed yielding scenario in time [Fig. 8(a)]. However, the various apparent conductivity responses exhibit significant differences: in the early stage of the experiment, all of the apparent conductivity responses start at the same value, but the conductivity measured for larger gaps increases more rapidly [Fig. 8(b)]. To determine the bulk contribution, we estimate the contact resistance by extrapolating the apparent conductivity in the limit $t = 0$ s. Then, using Eq. (4), we compute the bulk conductivity σ_b for each experiment. This computation is then further normalized by the gap height H [the inset in Fig. 8(b)].

In the entire primary-creep regime ($t \lesssim 50$ s), we observe that σ_b/H is independent of the gap height, which demonstrates that the increase in apparent conductivity during the primary-creep regime is due to a change in the bulk properties of the sample. The deformation of the sample microstructure under external stress appears to be sufficient to trigger the pairing of attractive CB particles, leading to an enhanced connectivity and, thus, a larger

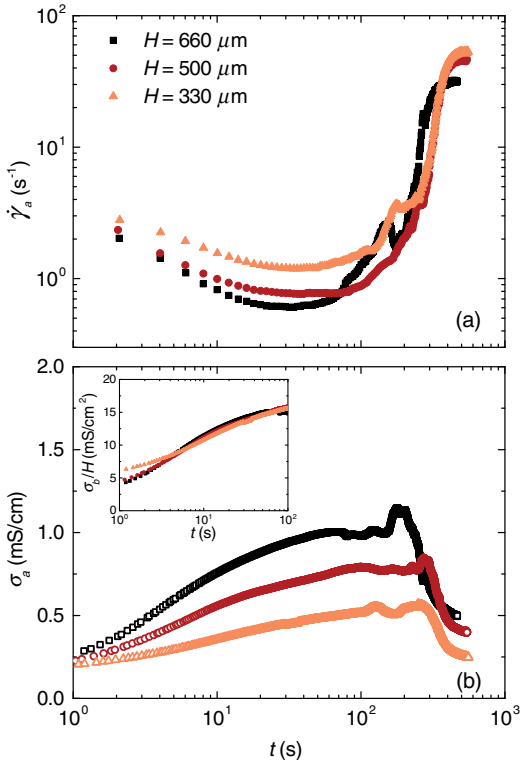

FIG. 8. Creep experiment in a carbon-black VXC72R suspension ($c = 8$ wt %) at $\tau = 30$ Pa for different gaps ($H = 660$, 500, and 330 μm). (a) Shear-rate response $\dot{\gamma}(t)$. (b) Apparent conductivity response $\sigma_a(t)$. (Inset) Estimated bulk conductivity $\sigma_b(t)$ normalized by the gap H. The contribution of the contact resistance is estimated using Eq. (4) and the measurements at multiple gaps for $t = 0$ s.

conductivity. In that framework, the faster increase of the conductivity at a larger gap can be interpreted as an increasing rate of plastic rearrangements for larger gaps.

To conclude this section, simultaneous time-resolved rheoelectric measurements provide a more detailed picture of the yielding scenario, which is in general agreement with previous velocimetry measurements [46,47]. As a key alternative result, time-resolved measurements of the conductivity during the primary-creep regime allow us to reveal the existence of stress-induced bulk rearrangements in the sample microstructure, which correspond to very small values of the macroscopic imposed strain.

C. Steady-state measurements

After studying the transient rheoelectric behavior of CB gels, we now focus on steady-state shear measurements. The determination of the true constitutive equation is crucial for numerous applications where the true bulk behavior must be accurately modeled [29,30,40,44,49–51], whereas numerous studies in the literature report only approximative or apparent flow curves [43–45]. In this last section, we take advantage of the rheoelectric test fixture to characterize accurately the constitutive rheological

behavior, together with the conductivity of CB gels, under flow by taking into account the inhomogeneity inherent to the parallel-plate geometry, the slip of the sample at the wall and the contact resistance.

A stress ramp of decreasing values from $\tau = 100$ to 0 Pa and composed of $N = 100$ steps, each of duration $\Delta t = 30$ s is performed on an 8-wt % CB gel (VXC72R). The choice of ramping the stress downwards and at a slow enough pace is made to ensure that the rheological and electrical properties are close to steady state at all shear rates explored. The resulting flow and conductivity curves, as well as the effects of the different corrections detailed below, are shown in Fig. 9(a).

We first discuss the mechanical corrections. The shear rate $\dot{\gamma}$ is not homogeneous across the parallel plate but depends on the radial position r as $\dot{\gamma}(r) = r\Omega_{\rm rot}/H$, where $\Omega_{\rm rot}$ is the angular velocity of the upper plate. The corrected flow curve can be obtained using the apparent shear rate at the rim $\dot{\gamma}_{a,R} = R\Omega_{\rm rot}/H$ and by computing the stress at the rim τ_R by means of the following expression [60]:

$$\tau_R(\dot{\gamma}_{a,R}) = \frac{\mathcal{M}}{2\pi R^3}\left[3 + \frac{d\ln \mathcal{M}/2\pi R^3}{d\ln \dot{\gamma}_{a,R}}\right], \tag{5}$$

where $\mathcal{M}$ denotes the torque applied on the upper plate. This expression enables determination of the true flow curve for a complex fluid from measurements of the torque and its derivative. The corrected flow curve, pictured as filled triangles in Fig. 9(a) appears to be shifted towards lower stresses for $\dot{\gamma} \leq 7$ s^{-1}.

Alternatively, single-point determination methods can also be used to correct for shear inhomogeneity to avoid additional noise associated with a numerical calculation of the derivative in Eq. (5) [71,72]. These methods rely on calculating the apparent Newtonian viscosity at the rim $\eta_N = 2\mathcal{M}H/\pi R^4\Omega_{\rm rot}$, which is then associated with a lower shear rate, equal to approximately three quarters of the rim shear rate. For Bingham plastic and power-law materials, the error associated with performing this single-point correction is typically less than 2% [71,72]. Indeed, the result of the latter method is barely distinguishable from that of the exact analytical expression given by Eq. (5) [inverted filled triangle in Fig. 9(a)].

Finally, correction for slip can be performed by conducting rheological measurements at different gaps [54,73,74]. If the flow curves obtained at various gaps superimpose, the material does not slip, whereas a gap-dependent rheology is the signature of wall slip. Assuming symmetric slip at both walls, the following kinematic relationship can be derived for a given imposed stress τ [54]:

$$\dot{\gamma}_a(\tau) = \dot{\gamma}_t(\tau) + \frac{2V_s(\tau)}{H}, \tag{6}$$

where $\dot{\gamma}_a$ is the apparent shear rate, $\dot{\gamma}_t$ the true shear rate, and V_s the slip velocity.

Experiments conducted at different gaps (see Fig. 15 in Appendix A) together with Eq. (6) allow us to compute the true flow curve of the carbon-black gel [filled squares in Fig. 9(a)]. The corrections reveal that the gel exhibits a critical shear rate of about 1 s^{-1}, below which no homogeneous flow is possible (see the additional discussion below regarding the formation of log-rolling flocs) and where, for shear stresses larger than 50 Pa, the shear rate is underestimated prior to the shear-inhomogeneity correction.

We now turn to the electric measurements and discuss the corrections to the apparent conductivity defined in Eq. (1), which is observed to decrease with an increasing shear rate [Fig. 9(b)]. First, following a calculation analogous to the one that leads to Eq. (5), an exact expression enabling correction for shear inhomogeneity can be derived for the conductivity (see the details in

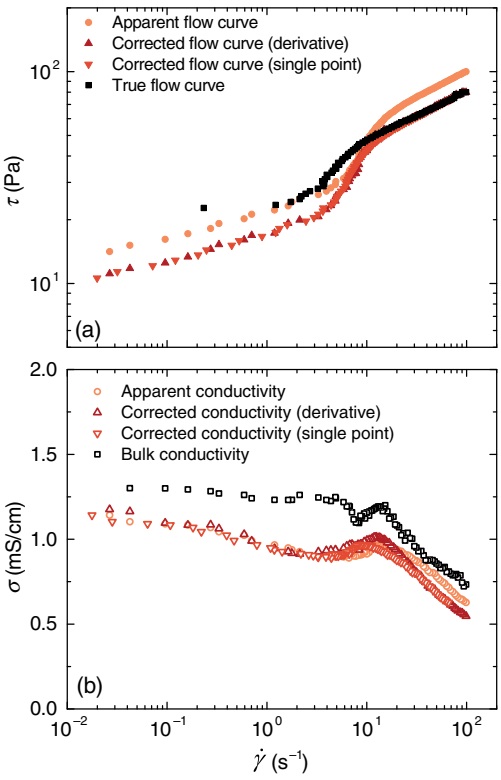

FIG. 9. Steady-state flow and conductivity curves in an 8-wt % carbon-black gel (VXC72R). (a) Flow curves showing the effects of the shear-inhomogeneity correction (derivative and single-point methods) as well as the slip correction. The "corrected" flow curves are obtained after correcting for shear inhomogeneity alone, while the true flow curve is obtained after correcting for both shear-inhomogeneity and slip effects. (b) Conductivity curves showing the effects of the shear-inhomogeneity correction as well as the contact-resistance correction. The corrected conductivity curves are obtained after correcting for shear inhomogeneity alone, while the bulk-conductivity curve is obtained after correcting for both shear-inhomogeneity and contact-resistance effects.

Appendix B 1), which reads, for the apparent conductivity $\sigma_{a,R}$ at the rim,

$$\sigma_{a,R}(\dot{\gamma}_{a,R}) = \frac{I}{\phi_0}\frac{H}{2\pi R^2}\left[2 + \frac{d\ln(\frac{I}{\phi_0}\frac{H}{2\pi R^2})}{d\ln\dot{\gamma}_{a,R}}\right], \qquad (7)$$

where I denotes the measured current and ϕ_0 the applied potential. Corrected data appears as simply shifted along the shear-rate axis [$\triangle$ in Fig. 9(b)]. Moreover, an analogous calculation to the single-point-determination method described in Refs. [71,72] leads to a similar expression for the conductivity (see the details in Appendix B 2).

The apparent conductivity defined in Eq. (1) is associated with a lower shear rate, equal to approximately two thirds of the shear rate at the rim. Here again, similarly to the rheological correction, the result of this method is barely distinguishable from that of the derivative method [inverted open triangle in Fig. 9(b)]. Finally, the expression for the contact resistance shown in Eq. (4), which is the electrical equivalent to the correction for slip [Eq. (6)] can be extended to a sample under flow (see Appendix B 3). For a given stress at the rim τ_R, one can thus write the resulting resistivity as

$$\frac{1}{\sigma_{a,R}(\tau_R)} = \frac{1}{\sigma_{b,R}(\tau_R)} + \frac{\rho_{c,R}(\tau_R)}{H}, \qquad (8)$$

where $\sigma_{a,R}$ denotes the measured apparent conductivity derived in Eq. (6) and $\sigma_{b,R}(\tau_R)$ is the bulk conductivity at the level of imposed stress τ_R.

Finally, $\rho_{c,R}$ is the specific contact resistance at the rim expressed in $\Omega\,\mathrm{cm}^2$ and defined as $\rho_{c,R}(\tau_R) = (\partial\mathcal{R}_c/\partial j)_R(\tau_R)$, where $\mathcal{R}_c$ is the contact resistance and j is the current density. By introducing the specific contact resistance, Eq. (8) takes into account the potential variation of the contact resistance with the radius r and hence its dependence on both the shear rate and the shear stress. Ultimately, we find that the fully corrected conductivity curve shows the same trend as the raw data but is quantitatively shifted towards larger conductivities [open square in Fig. 9(b)].

Experiments conducted at different gaps (see Fig. 16 in Appendix B) together with Eq. (8) allow us to compute the bulk conductivity of the carbon-black gel [open square in Fig. 9(b)]. Let us now discuss the quantities extracted from both the mechanical and electrical corrections of the flow curve, i.e., the slip velocity V_s, the bulk conductivity σ_b, and the specific contact resistance ρ_c. These quantities are reported as a function of the applied stress τ in Fig. 10 during the flow cessation of an 8-wt % CB gel (VXC72R).

Consequently, the graphs in Fig. 10 should be read from right to left. At large stresses, i.e., $\tau \geq 75$ Pa, the slip velocity is negligible, and the bulk resistance and specific contact resistance are constant, in agreement with a fully fluidized sample that is sheared homogeneously. As the stress is ramped down to $\tau \simeq 55$ Pa, the bulk conductivity

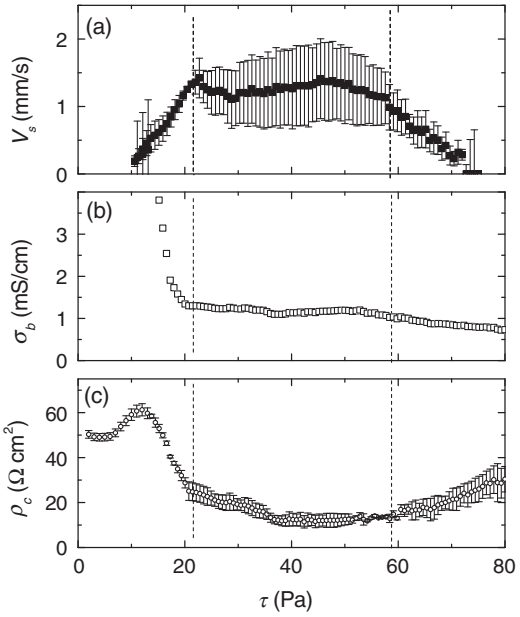

FIG. 10. Slip velocity V_s, bulk conductivity σ_b, and specific contact resistance ρ_c obtained from the slip and contact-resistance corrections performed on the steady-state flow curves in an 8-wt % carbon-black gel (VXC72R). The vertical dashed lines indicate the limits of the three regimes discussed in the text. Displayed from large to low stresses, the fully fluidized regime for $\tau \geq 55$ Pa, the plug flow with slip at the walls for 55 Pa $\geq \tau \geq$ 20 Pa, and the shear-induced structuration (the formation of vorticity-aligned flocs) for $\tau \leq 20$ Pa are shown. (a) Slip velocity $V_s(\tau)$. (b) Bulk conductivity $\sigma_b(\tau)$. (c) Specific contact resistance $\rho_c(\tau)$.

slowly increases and the slip velocity becomes positive, while the specific contact resistance decreases.

These evolutions reflect the aggregation of the CB particles into larger flocs, which better conduct the current and display an increasing amount of slip at the wall. Such aggregates experience more contact with the wall than individual CB particles—hence the decrease in ρ_c. From $\tau \simeq 55$ to 20 Pa, both σ_b and V_s are roughly constant, while ρ_c slowly increases as the stress is ramped down. These results strongly suggest the appearance of thin lubrication layers at both walls, mainly composed of oil and isolating a bulk percolated structure of CB particles that is only weakly sheared. Moreover, assuming a slip layer of thickness δ and viscosity η_s that is equal to the value for the matrix phase, the stress at the wall reads [8] $\tau_w = \eta_s V_s/\delta$, where V_s/δ denotes the shear rate inside the slip layer. As both V_s and δ remain constant with a decreasing stress, one should expect the thickness δ of the slip layer to progressively increase from $\delta \simeq 400$ nm to 1 μm. Indeed, the specific contact resistance increases concomitantly with the stress decrease.

Finally, for $\tau \leq 20$ Pa, both the bulk conductivity and the contact resistance show a dramatic increase, which is the signature of strong changes in the sample microstructure that we interpret as the formation of vorticity-aligned flocs

[17,18,75]. Indeed, the formation of log-rolling flocs has been reported in confined geometries for shear rates lower than a critical value $\dot{\gamma}_c$ that scales for VXC72R CB gels as $\dot{\gamma}_c = 3650/H^{1.4}$, with H given in micrometers, independently of the CB concentration [18].

For $H = 750$ μm, one calculates $\dot{\gamma}_c \simeq 1.2$ s^{-1}, which, according to the true flow curve of the gel [Fig. 9(a)], corresponds to $\tau_c \simeq 25$ Pa, in good agreement with the transition observed in Fig. 10 at $\tau \simeq 20$ Pa. Therefore, at low shear rates, the rheoelectric measurements reflect the growth of a shear-induced structure which is otherwise hard to visualize at such large concentrations of CB [18].

The above analysis shows that conclusions drawn from rheoelectric measurements must be considered with care, and, we highlight the importance of corrections for shear inhomogeneity in parallel-plate geometry, wall slip and contact resistance, which are often overlooked in the study of strongly conductive complex fluids. Application of these corrections also provides quantitative values for important quantities—namely, the slip velocity, bulk conductivity, and specific contact resistance—which, once combined, provide a more complete picture of the flow profile in the conductive gel at steady state over a large range of stress values.

IV. DISCUSSION

The rheoelectric apparatus described in Sec. II provides robust measurements for highly conductive materials at rest, during transient flows, and under steady-state shear.

Flow-cessation experiments on carbon-black gels reported in Sec. III A have revealed that the sample shearing history tunes concomitantly the elastic and electric properties of these attractive gels. Progressive stress decrease down to $\tau = 0$ Pa leads to a more solidlike gel whose elastic modulus G_0' varies as a power-law function of the conductivity σ_0 for increasing quenching speed: i.e., $G_0' \propto \sigma_0^{\alpha}$, with $\alpha = 1.65 \pm 0.04$.

Previous measurements on gels formulated with the exact same carbon-black powder from Cabot at various volume fractions ϕ have shown that $G_0' \propto (\phi - \phi_c)^{\nu}$, with $\nu = 4.0 \pm 0.1$, where the exponent ν is consistent with percolation theory [66]. Assuming that the electrical and elastic percolation occurs at the same volume fraction ϕ_c, one can expect from the measurements reported here that $\sigma_0 \propto (\phi - \phi_c)^t$, with $t = \nu/\alpha = 2.4 \pm 0.1$ [76]. Interestingly, we find $t < \nu$, which is in qualitative agreement with theoretical predictions obtained using lattice models [70]. However, this value of t is quantitatively outside the range of values predicted by percolation theories $1.5 \leq t \leq 2$ [77–79], and larger than values recently reported for other carbon-black gels: Ketjenblack ($t = 1.9$) and Super C-45 ($t = 1.7$), dispersed in an organic solvent [44].

These results can be interpreted in light of previous studies on solid polymer composites loaded with carbon-black particles. Indeed, insulating plastics loaded with carbon-black particles show conductive properties that increase as a power law of the carbon-black content, and the exponent depends on the shape of the carbon-black particles [80]. Highly structured or fractal-like particles such as Ketjenblack display a narrow distribution of interparticle tunneling distances and exhibit "universal" behavior; i.e., the scaling exponent of the conductivity with the packing fraction is $t = 2$, in agreement with percolation theories.

For less structured or smoother carbon-black particles (but those that are still more tortuous than perfect spheres), the conductivity is lower in absolute value but increases faster with the volume fraction [81,82]. Interestingly, Balberg reported an exponent of $t = (2.8 \pm 0.2) > 2$ for Cabot carbon-black particles embedded in a solid PVC matrix [80]. Here, we also find that $t = 2.4$ for carbon-black gels composed of the same carbon-black particles, which strongly suggests that the conduction mechanism proposed for VXC72R carbon-black particles embedded in solid composites also holds true for carbon-black gels in a nonaqueous solvent.

We also show in Sec. III B that the rheoelectric apparatus is well adapted to probe the evolution of the gel structure under weak deformations and provides much higher sensitivity for monitoring the evolution of the microstructure compared to other techniques, such as velocimetry [47]. Indeed, applied to creep experiments, rheoelectric measurements reveal that the power-law response of the carbon-black gel during the primary-creep regime is associated with an increase in the network connectivity and conductivity of the gel.

Power-law responses to creep tests have been reported already for numerous other soft materials, such as microgels [83], polycrystalline-surfactant hexagonal phases [84], core-shell colloidal particles [85], and protein gels [86,87]. However, the present measurements are among the first to illustrate the existence of simultaneous rearrangements of the sample in bulk.

At the strand level, such rearrangements may likely correspond to the net creation of new bonds due to the presence of attractive van der Waals forces between the soot particles. Indeed, recent numerical simulations on model colloidal gels have revealed that imposed macroscopic deformation leads to the formation of new bonds, even at low strain [88], which may account for the increase in conductivity reported in Fig. 8.

More simulations under applied shear-stress conditions are needed to clarify the evolution of the sample network connectivity during primary creep. We also emphasize that there is currently no quantitative theoretical description for the evolution of the gel microstructure during fluidization, and that our experimental measurements of the evolution in both stress and conductivity during the fluidization process provide a data set to help test predictions of future models.

In steady shear, we show in Sec. III C that performing corrections for shear inhomogeneity, wall slip, and contact

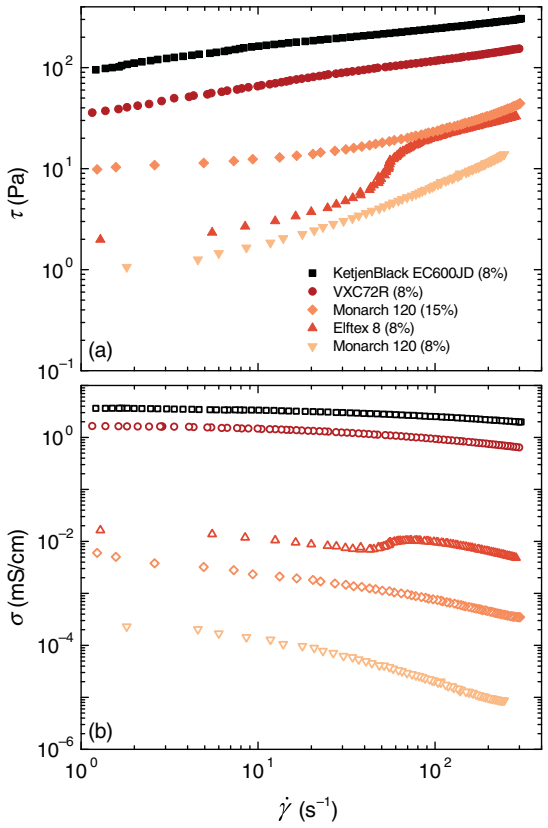

FIG. 11. Sets of corrected (a) flow curves and (b) conductivity curves for carbon-black gels made with carbon-black particles of different grades: Ketjenblack EC600JD, VXC72R, Elftex 8 at weight concentration $c = 8$ wt %, and Monarch 120 at $c = 8$ and 15 wt %.

resistance are crucial to correctly determine the electrical and mechanical constitutive behavior of CB gels under flow. As a result, we can now safely compare the rheoelectric properties of CB gels made from different grades of carbon black. We examine 8-wt % CB gels made, respectively, of VXC72R, Monarch 120, Elftex 8 (Cabot), and Ketjenblack EC600JD (Akzo Nobel), as well as a 15-wt % dispersion made of Monarch 120 (Cabot).

Similarly to the experiments reported in Fig. 5, ramps of decreasing stress from $\tau = \tau_{\max}$ down to $\tau = 0$ Pa and composed of $N = 100$ steps each of duration $\Delta t = 15$ s are applied to each gel. The value of $\tau_{\max}$, which ranges from 15 to 300 Pa depending on the type of CB gels, is chosen such that the corresponding shear rate is 300 s^{-1} for all samples (Fig. 11). The rheoelectric properties of the different 8-wt % CB gels span over several orders of magnitude in both conductivity and stress.

On the one hand, CB gels made with Ketjenblack EC600JD and VXC72R show a high conductivity larger than 1 mS/cm that is weakly sensitive to shear, which is indeed why these CB gels were initially designed. Such properties are intimately linked to their large specific surface area of about 200 m^2/g for the VXC72R sample [89,90] and 1400 m^2/g for the Ketjenblack EC600JD [49,50,89]. On the other hand, CB gels made with Elftex 8 and Monarch 120 display a much lower conductivity that is also more strongly sensitive to shear. Correspondingly, these CB gels have a lower specific surface area of about 75 m^2/g [91] and 29 m^2/g [92], respectively. Such CB gels are typically used for color as pigments, where CB conductive properties are less crucial.

Finally, we note that the electrical properties of these CB dispersions are strongly related to the individual properties of the CB particles. In particular, increasing the concentration in CB does not compensate for low conductivity values or shear sensitivity, as illustrated by the results for a gel made of 15 wt % of Monarch 120. These measurements illustrate how the rheoelectric fixture can be used to compare, rank, and select the desired properties of highly conductive complex fluids.

V. CONCLUSION

In this work, we introduce an alternative rheoelectric apparatus designed for conventional stress-controlled rheometers. This apparatus can be used to accurately measure the conductivity of strongly conductive materials under flow at the same time as the viscometric properties of the gel are measured. Benchmark tests on CB gels have allowed us to illustrate the high sensitivity of the apparatus—even at low strains—and to determine the transient and steady-state behavior of CB gels by comparing the simultaneous electrical and mechanical response.

Furthermore, by taking into account shear inhomogeneity, wall slip, and the existence of a measurable contact resistance, we show that the correction methods first introduced to extract true bulk mechanical measurements from parallel-plate rheometry data can be formally extended to analyze electrical data. The latter analysis should be used as a reference for future electrical characterization of conductive complex fluids, such as conductive silver pastes, carbon-nanotube nanocomposites, conductive inks, etc.

More generally, the low-friction rheoelectric apparatus we have designed for stress-controlled rheometers paves the way for a wider use of rheoelectrical measurements in the broad soft-matter community. In particular, the present apparatus enables two-electrode electrochemical tests to be performed under flow, which is of primary importance for flow batteries, where the systematic characterization of cell performance under flow in a controlled environment is crucial for cell design and optimization.

ACKNOWLEDGMENTS

The authors thank X.-W. Chen, Y.-M. Chiang, E. Del Gado, F. Fan, and S. Manneville for the insightful discussions, and TA Instruments for the technical advice. The authors acknowledge support from the Joint Center for Energy Storage Research (JCESR), an Energy Innovation

Hub funded by the U.S. Department of Energy and the Basic Energy Science (BES) program of the Office of Science (SC). Finally, the authors gratefully acknowledge support from the MIT-France seed fund and the CNRS through a PICS-USA scheme (No. 36939).

APPENDIX A: SUPPLEMENTAL EXPERIMENTS ON CARBON-BLACK GELS

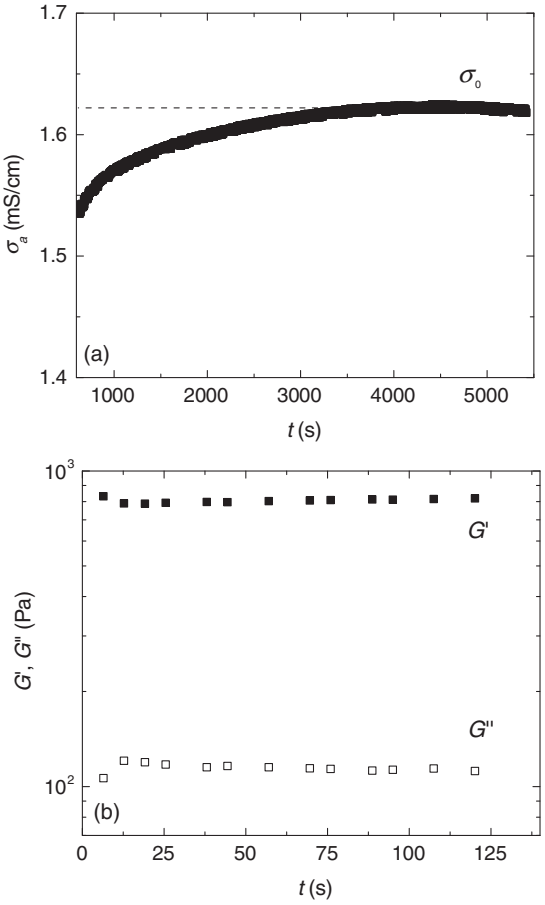

FIG. 12. (a) Temporal evolution of the apparent conductivity σ_a in an 8-wt % carbon-black gel (VXC72R) during the 90-min recovery period that follows a decreasing ramp of stress, from $\tau = 100$ Pa to $\tau = 0$ Pa. The stress and conductivity data associated with the ramp are pictured in Fig. 4 in the main text (duration per point, $\Delta t = 6$ s). The conductivity reaches a steady-state value $\sigma_0 = 1.62$ mS/cm after about an hour. (b) Viscoelastic moduli G' and G'' vs time, measured with oscillations of small amplitude ($\gamma_0 = 0.2\%$) at $\omega = 6.3$ rad/s, after the 90-min recovery period shown in (a). The viscoelastic moduli are constant with values $G'_0 = 805 \pm 4$ Pa, and $G''_0 = 114 \pm 6$ Pa. The values of σ_0 and G'_0 are reported in Fig. 6 in the main text, and they are further determined systematically for different ramp durations Δt in carbon-black gels of various concentrations to assemble the data set reported in Fig. 5 in the main text.

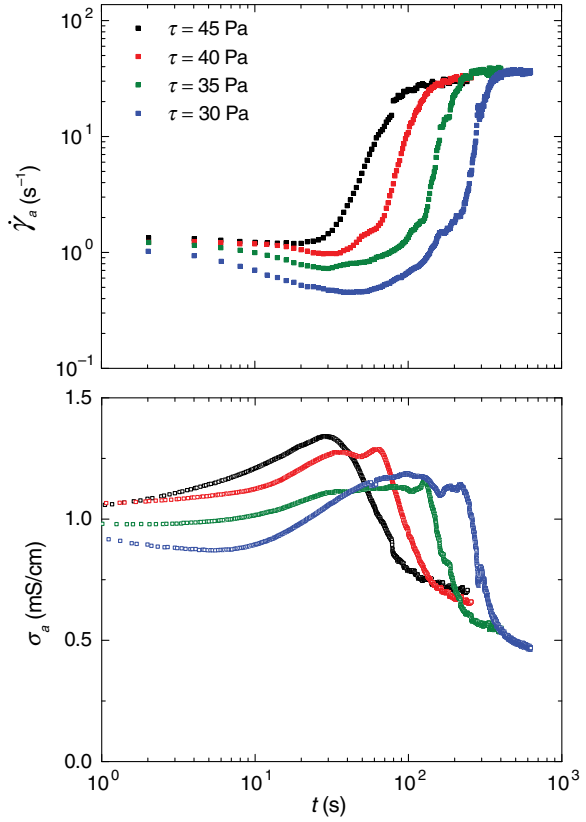

FIG. 13. Creep experiments in an 8-wt % carbon-black gel (VXC72R) at various stresses: $\tau = 45$, 40, 35, and 30 Pa. (a) Shear-rate response $\dot{\gamma}_a(t)$ and (b) apparent-conductivity response $\sigma_a(t)$. Before each experiment, the gel is presheared at $\dot{\gamma} = 200$ s^{-1} for 5 min to erase the previous flow history, then left to restructure for a waiting time $t_w = 1200$ s at $\tau = 0$ Pa.

APPENDIX B: DERIVATION OF ELECTRICAL CORRECTIONS IN THE PARALLEL PLATE

1. Shear inhomogeneity: Derivative method

In a parallel-plate geometry, the shear rate $\dot{\gamma}$ is not homogeneous across the gap but depends on the radial position r as $\dot{\gamma}(r) = r\Omega_{\rm rot}/H$, where $\Omega_{\rm rot}$ is the angular velocity of the upper plate and H is the sample gap. Shear inhomogeneity can be corrected by means of the shear rate at the rim $\dot{\gamma}_R = R\Omega_{\rm rot}/H$ and computing the stress at the rim τ_R using the following expression [60]:

$$\tau_R(\dot{\gamma}_R) = \frac{\mathcal{M}}{2\pi R^3}\left[3 + \frac{d\ln \mathcal{M}/2\pi R^3}{d\ln \dot{\gamma}_R}\right], \qquad \text{(B1)}$$

where $\mathcal{M}$ denotes the torque applied on the upper plate. A similar expression can be derived for electrical measurements. Indeed, the total current I that is measured is given by the following expression:

$$I = \frac{\phi_0}{H} 2\pi \int_0^R \sigma_a(r) r dr, \qquad \text{(B2)}$$

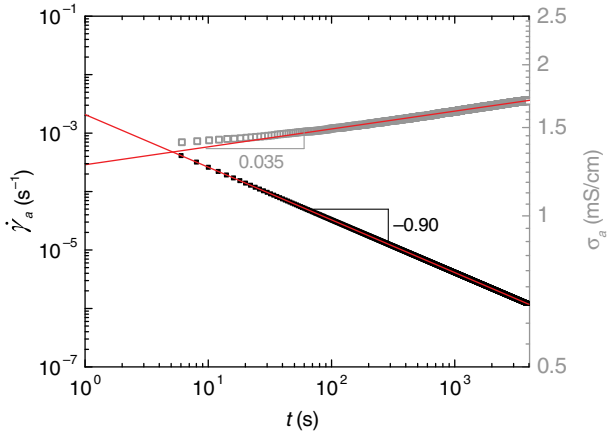

FIG. 14. Creep experiment in an 8-wt % carbon-black gel (VXC72R) at $\tau = 22$ Pa. Apparent shear-rate response $\dot{\gamma}_a(t)$ and apparent-conductivity response $\sigma_a(t)$ on doubly logarithmic scales to emphasize the power-law characteristics of the primary-creep regime. The same data is shown as that presented in Fig. 7(a). The shear rate is calculated numerically from the strain measured by the rheometer to increase the precision. The red lines correspond to the best power-law fits of the data, which leads to $\dot{\gamma}_a(t) = At^{\alpha}$, with $A = (2.3 \pm 0.1) \times 10^{-3}$ $s^{-\alpha-1}$ and $\alpha = -0.90 \pm 0.02$, and $\sigma_a(t) = Bt^{\beta}$, with $B = 1.26 \pm 0.01$ mS $s^{-\beta}$/cm and $\beta = 0.035 \pm 0.002$. We note that the power-law fit of the conductivity is hardly distinguishable from a logarithmic fit $\sigma_a(t) = C\ln(t) + D$ for the data under study, with $C = 0.0560 \pm 0.0005$ mS/cm and $D = 1.23 \pm 0.01$ mS/cm.

where ϕ_0 is the applied potential and σ_a is the apparent conductivity. By changing the integration variable from r to $\dot{\gamma}$, we obtain

$$I = \frac{\phi_0}{H}\frac{2\pi R^2}{\dot{\gamma}_R{}^2}\int_0^{\dot{\gamma}_R}\sigma_a(\dot{\gamma})\dot{\gamma}d\dot{\gamma}. \tag{B3}$$

Differentiating this result with respect to $\dot{\gamma}_R$ while using the Leibniz formula leads to

$$\frac{dI}{d\dot{\gamma}_R} = \frac{-2I}{\dot{\gamma}_R} + \frac{\phi_0}{H}\frac{2\pi R^2}{\dot{\gamma}_R}\sigma_{a,R}(\dot{\gamma}_R), \tag{B4}$$

which can be rewritten as

$$\sigma_{a,R}(\dot{\gamma}_R) = \left(\frac{H}{2\pi R^2}\frac{I}{\phi_0}\right)\left[2 + \frac{d\ln(\frac{H}{2\pi R^2}\frac{I}{\phi_0})}{d\ln\dot{\gamma}_R}\right]. \tag{B5}$$

The latter expression relates the apparent conductivity at the rim of the plate $\sigma_{a,R}$ to the macroscopic current I measured at a shear rate $\dot{\gamma}_R = R\Omega_{\rm rot}/H$. Equation (B5) allows us to correct for the radial-shear inhomogeneity in the parallel-plate geometry.

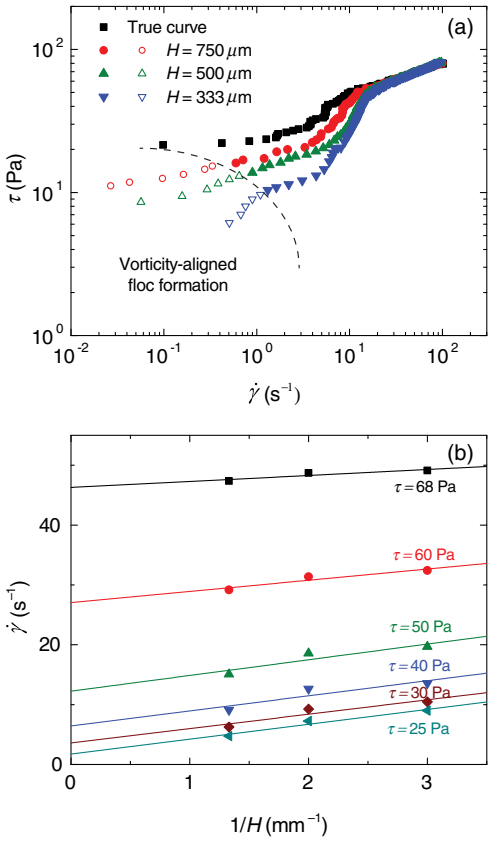

FIG. 15. (a) Flow curves of an 8-wt % carbon-black gel (VXC72R) measured for various gap heights, $H = 750$, 500, and 330 μm, together with the true flow curve corrected for slip. The open symbols indicate the region associated with the formation of vorticity-aligned flocs. The boundary for the onset of this regime is given by $\dot{\gamma}_c = 3650/H^{1.4}$, with H given in micrometers, independently of the CB concentration [18]. (b) Plot of the measured values of apparent shear rate $\dot{\gamma}_a$ vs $1/H$ for various imposed stresses: $\tau = 68$, 60, 50, 40, 30, and 25 Pa. The colored lines correspond to the best linear fits of the data and allow us to extract the true shear rate $\dot{\gamma}_t$ and the slip velocity V_s for each imposed stress τ using Eq. (6).

2. Shear inhomogeneity: Single-point method

The single-point correction method relies on the Gaussian quadrature of moments equation which takes the following form [72]:

$$\int_0^1 f(x)x^k dx = \sum_{i=1}^{n} w_i f(x_i), \tag{B6}$$

where k and n denote integers larger than 1 and the pairs $\{w_i, x_i\}$ are given in Ref. [93]. In the parallel-plate geometry, the torque $\mathcal{M}$ can be expressed as an integral:

$$\mathcal{M} = 2\pi\int_0^R \tau(r)r^2 dr. \tag{B7}$$

The integral can be nondimensionalized by replacing the integration variable r by $x = \dot{\gamma}/\dot{\gamma}_R = r/R$. We obtain

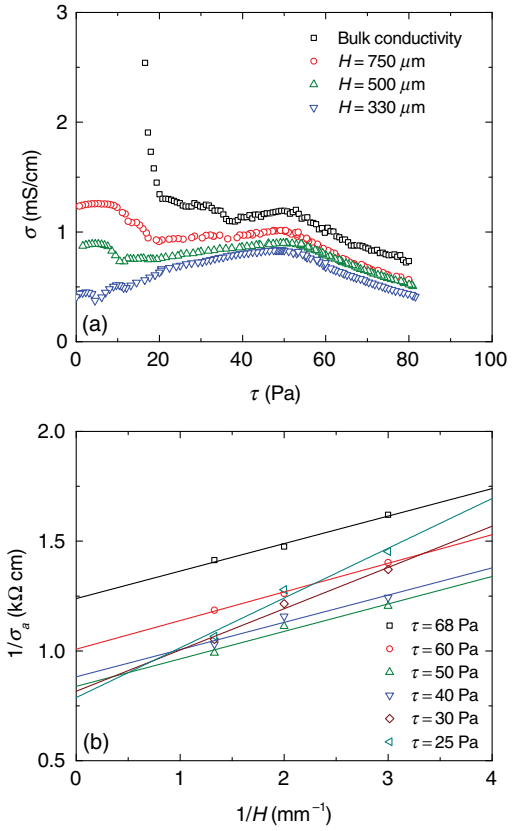

FIG. 16. (a) Conductivity curves of an 8-wt % carbon-black gel (VXC72R) measured for various gap heights, $H = 750$, 500, and 330 μm, together with the bulk-conductivity curve. (b) Inverse of the apparent resistivity $1/\sigma_a$ vs $1/H$ for various stresses: $\tau = 68$, 60, 50, 40, 30, and 25 Pa. The colored lines correspond to the best linear fits of the data and allow us to extract the bulk resistivity $1/\sigma_b$ and the specific contact resistance ρ_c for each stress τ using Eq. (8).

$$\mathcal{M} = 2\pi R^3 \int_0^1 \tau(x) x^2 dx. \tag{B8}$$

By using Eq. (B6) with $n = 1$ and $k = 2$, we compute $\{w_1, x_1\} = \{1/3, 3/4\}$, which leads to

$$\mathcal{M} \simeq 2\pi R^3 \frac{\tau(r = 3R/4)}{3}, \tag{B9}$$

otherwise written as

$$\tau\left(\frac{3\dot{\gamma}_R}{4}\right) \simeq \frac{3\mathcal{M}}{2\pi R^3}. \tag{B10}$$

Equation (B10) links the stress at $r = 3R/4$ to the torque $\mathcal{M}$. The error associated with Eq. (B10) is generally less than 5% for Bingham plastic and Newtonian fluids [72]. Moreover, an expression similar to Eq. (B8) can be derived for electrical measurements. Indeed, we can express the macroscopic current as follows:

$$I = \frac{\phi_0 2\pi R^2}{H} \int_0^1 \sigma_a(x) x dx. \tag{B11}$$

Again using Eq. (B6) with $n = 1$ and $k = 1$, we find that $\{w_i, x_i\} = \{1/2, 2/3\}$, and thus that

$$I \simeq \frac{\phi_0 \pi R^2}{H} \sigma_a(r = 2R/3), \tag{B12}$$

which leads to the following expression:

$$\sigma_a\left(\frac{2\dot{\gamma}_R}{3}\right) \simeq \frac{IH}{\phi_0 \pi R^2}, \tag{B13}$$

which relates the apparent conductivity at $r = 2R/3$ to the macroscopic current I at a rotation rate $\Omega_{\rm rot}$ and a gap H. The static apparent conductivity given by the value of $(IH/\phi_0 \pi R^2)$ is thus associated with the shear rate $2\dot{\gamma}_R/3 = 2\Omega_{\rm rot} R/3H$.

3. Contact-resistance correction

Viscometric corrections for wall slip can be performed by conducting rheological measurements at different gaps [54,73,74]. If the flow curves obtained at various gaps superimpose, the material does not slip, whereas a gap-dependent rheology is the signature of wall slip. Assuming symmetric slip at both walls, the following kinematic relationship can be derived for a given imposed stress τ [54]:

$$\dot{\gamma}_a(\tau) = \dot{\gamma}_t(\tau) + \frac{2V_s(\tau)}{H}, \tag{B14}$$

where $\dot{\gamma}_a$ is the apparent shear rate, $\dot{\gamma}_t$ is the true shear rate, and V_s denotes the slip velocity. In the case of a static measurement of conductivity, the apparent conductivity σ_a measured experimentally is the sum of a bulk contribution σ_b and a contact resistance $\mathcal{R}_c$ originating from the two interfaces:

$$\mathcal{R}_{\rm measured} \equiv \frac{\phi_0}{I} = \frac{H}{\sigma_a \pi R^2} = \mathcal{R}_c + \frac{H}{\sigma_b \pi R^2}. \tag{B15}$$

To extend the latter correction to a sample flowing in the parallel-plate geometry, we consider an annulus of width dr at a radius r and define the specific contact resistance at radius r as $\rho_c(r) = [\partial \mathcal{R}_c(r)/\partial j]$, where $\mathcal{R}_c$ is the contact resistance at a radius r and $j = I/\pi R^2$ is the current density. In this annular ring, the incremental conductance can be written as

$$d\mathcal{G}(r) = \frac{2\pi r dr}{\rho_c(r)} + \frac{\sigma_b(r) 2\pi r dr}{H} \tag{B16}$$

and the current as

$$dI(r) = \phi_0 d\mathcal{G}(r) = \frac{\phi_0 r dr}{\frac{\rho_c(r)}{2\pi} + \frac{H}{\sigma_b(r)2\pi}}. \quad \text{(B17)}$$

Summing the above expressions, the resistance of each component adds in parallel and the macroscopic current measured reads

$$I = \int_0^R \frac{2\pi\phi_0 r dr}{\rho_c(r) + \frac{H}{\sigma_b(r)}}. \quad \text{(B18)}$$

Furthermore, following the same derivation as for the rheometrical correction [see Eqs. (B2), (B3), and (B4)], we obtain

$$\sigma_{a,R} = \frac{H}{2\pi R^2}\frac{I}{\phi_0}\left[2 + \frac{d\ln\left(\frac{H}{2\pi R^2}\frac{I}{\phi_0}\right)}{d\ln\dot{\gamma}_R}\right] = \frac{1}{\frac{\rho_{c,R}}{H} + \frac{1}{\sigma_{b,R}}}. \quad \text{(B19)}$$

In summary, by analogy to the slip correction in Eq. (B14), for a given imposed stress at the rim τ_R as defined by Eq. (B1), we can decouple the bulk contribution from the surface contribution to the conductivity as follows:

$$\frac{1}{\sigma_{a,R}(\tau_R)} = \frac{\rho_{c,R}(\tau_R)}{H} + \frac{1}{\sigma_{b,R}(\tau_R)}. \quad \text{(B20)}$$

Alternatively, if we use single-point determination methods to compute the apparent conductivity, we can derive the following relation:

$$\frac{1}{\sigma_a[\tau(\frac{2\dot{\gamma}_R}{3})]} = \frac{\rho_c[\tau(\frac{2\dot{\gamma}_R}{3})]}{H} + \frac{1}{\sigma_b[\tau(\frac{2\dot{\gamma}_R}{3})]}. \quad \text{(B21)}$$

We note that Eq. (B21) is useful only if the full flow curve is known (e.g., from a stress sweep), as information about the quantity $\tau(2\dot{\gamma}_R/3)$ at a shear rate $\dot{\gamma} = 2\dot{\gamma}_R/3$ is unknown *a priori* since $\tau(3\dot{\gamma}_R/4)$ is the quantity obtained from the single-point determination method applied to the rheological data.

[1] N. J. Balmforth, I. A. Frigaard, and G. Ovarlez, Developments in viscoplastic fluid mechanics, Annu. Rev. Fluid Mech. **46**, 121 (2014).

[2] G. H. McKinley, A hitchhikers guide to complex fluids, Rheology bulletin **84**, 14 (2015).

[3] P. J. Lu and D. A. Weitz, Colloidal particles: Crystals, glasses, and gels, Annu. Rev. Condens. Matter Phys. **4**, 217 (2013).

[4] P. Coussot, Rheophysics of pastes: A review of microscopic modelling approaches, Soft Matter **3**, 528 (2007).

[5] M.-A. Fardin and S. Lerouge, Instabilities in wormlike micelle systems, Eur. Phys. J. E **35**, 91 (2012).

[6] T. Divoux, M.-A. Fardin, S. Manneville, and S. Lerouge, Shear banding of complex fluids, Annu. Rev. Fluid Mech. **48**, 81 (2016).

[7] G. Ovarlez, S. Rodts, X. Chateau, and P. Coussot, Phenomenology and physical origin of shear localization and shear banding in complex fluids, Rheol. Acta **48**, 831 (2009).

[8] H. A. Barnes, A review of the slip (wall depletion) of polymer solutions, emulsions and particle suspensions in viscometers: Its cause, character, and cure, J. Non-Newtonian Fluid Mech. **56**, 221 (1995).

[9] D. M. Kalyon, Apparent slip and viscoplasticity of concentrated suspensions, J. Rheol. **49**, 621 (2005).

[10] R. Buscall, Letter to the editor: Wall slip in dispersion rheometry, J. Rheol. **54**, 1177 (2010).

[11] M.-A. Fardin, T. J. Ober, V. Grenard, T. Divoux, S. Manneville, G. H. McKinley, and S. Lerouge, Interplay between elastic instabilities and shear-banding: Three categories of Taylor-Couette flows and beyond, Soft Matter **8**, 10072 (2012).

[12] J. Persello, A. Magnin, J. Chang, J. M. Piau, and B. Cabane, Flow of colloidal aqueous silica dispersions, J. Rheol. **38**, 1845 (1994).

[13] F. Pignon, A. Magnin, and J.-M. Piau, Thixotropic colloidal suspensions and flow curves with minimum: Identification of flow regimes and rheometric consequences, J. Rheol. **40**, 573 (1996).

[14] J. V. DeGroot, C. W. Macosko, T. Kume, and T. Hashimoto, Flow-induced anisotropic SALS in silica-filled PDMS liquids, J. Colloid Interface Sci. **166**, 404 (1994).

[15] A. Montesi, A. A. Peña, and M. Pasquali, Vorticity Alignment and Negative Normal Stresses in Sheared Attractive Emulsions, Phys. Rev. Lett. **92**, 058303 (2004).

[16] C. O. Osuji, C. Kim, and D. A. Weitz, Shear thickening and scaling of the elastic modulus in a fractal colloidal system with attractive interactions, Phys. Rev. E **77**, 060402(R) (2008).

[17] A. S. Negi and C. O. Osuji, New insights on fumed colloidal rheology—Shear thickening and vorticity-aligned structures in flocculating dispersions, Rheol. Acta **48**, 871 (2009).

[18] V. Grenard, N. Taberlet, and S. Manneville, Shear-induced structuration of confined carbon black gels: Steady-state features of vorticity-aligned flocs, Soft Matter **7**, 10 (2010).

[19] S. Pujari, S. Rahatekar, J. W. Gilman, K. K. Koziol, A. H. Windle, and W. R. Burghardt, Shear-induced anisotropy of concentrated multiwalled carbon nanotube suspensions using x-ray scattering, J. Rheol. **55**, 1033 (2011).

[20] A. P. R. Eberle and L. Porcar, Flow-SANS and Rheo-SANS applied to soft matter, Curr. Opin. Colloid Interface Sci. **17**, 33 (2012).

[21] D. Bonn, S. Rodts, M. Groenink, S. Rafaï, N. Shahidzadeh-Bonn, and P. Coussot, Some applications of magnetic resonance imaging in fluid mechanics: Complex flows and complex fluids, Annu. Rev. Fluid Mech. **40**, 209 (2008).

[22] P. T. Callaghan, Rheo NMR and shear banding, Rheol. Acta **47**, 243 (2008).

[23] B. Rajaram and A. Mohraz, Microstructural response of dilute colloidal gels to nonlinear shear deformation, Soft Matter **6**, 2246 (2010).

[24] S. Manneville, Recent experimental probes of shear banding, Rheol. Acta **47**, 301 (2008).
[25] T. Gallot, C. Perge, V. Grenard, M.-A. Fardin, N. Taberlet, and S. Manneville, Ultrafast ultrasonic imaging coupled to rheometry: Principle and illustration, Rev. Sci. Instrum. **84**, 045107 (2013).
[26] J. Mewis, L. M. de Groot, and J. A. Helsen, Dielectric behaviour of flowing thixotropic suspensions, Colloids Surf. **22**, 249 (1987).
[27] U. Genz, J. A. Helsen, and J. Mewis, Dielectric spectroscopy of reversibly floculated dispersions during flow, J. Colloid Interface Sci. **165**, 212 (1994).
[28] S. Capaccioli, D. Prevosto, A. Best, A. Hanewald, and T. Pakula, Applications of the rheo-dielectric technique, J. Non-Cryst. Solids **353**, 4267 (2007).
[29] W. Bauhofer, S. C. Schulz, A. E. Eken, T. Skipa, D. Lellinger, I. Alig, E. J. Tozzi, and D. J. Klingenberg, Shear-controlled electrical conductivity of carbon nanotubes networks suspended in low and high molecular weight liquids, Polymer **51**, 5024 (2010).
[30] I. Alig, D. Pötschke, D. Lellinger, T. Skipa, S. Pegel, G. R. Kasaliwal, and T. Villmow, Establishment, morphology and properties of carbon nanotube networks in polymer melts, Polymer **53**, 4 (2012).
[31] T. Amari, Flow properties and electrical conductivity of carbon black-linseed oil suspension, J. Rheol. **34**, 207 (1990).
[32] J. Crawshaw and G. Meeten, Shear-induced changes of electrical conductivity in suspensions, Rheol. Acta **46**, 183 (2006).
[33] H. Watanabe, T. Sato, K. Osaki, M.-L. Yao, and A. Yamagishi, Rheological and dielectric behavior of a styrene-isoprene-styrene triblock copolymer in selective solvents. 2. Contribution of loop-type middle blocks to elasticity and plasticity, Macromolecules **30**, 5877 (1997).
[34] H. Watanabe, T. Sato, Y. Matsumiya, T. Inoue, and K. Osaki, Rheo-dielectrics: Its applicability, Nihon Reoroji Gakkaishi **27**, 121 (1999).
[35] N. Lou, Y. Wang, X. Li, H. Li, P. Wang, C. Wesdemiotis, A. P. Sokolov, and H. Xiong, Dielectric relaxation and rheological behavior of supramolecular polymeric liquid, Macromolecules **46**, 3160 (2013).
[36] X. D. Pan and G. H. McKinley, Simultaneous measurement of viscoelasticity and electrical conductivity of an electrorheological fluid, Langmuir **14**, 985 (1998).
[37] I. Alig, T. Skipa, M. Engel, D. Lellinger, S. Pegel, and P. Pötschke, Electrical conductivity recovery in carbon nanotube-polymer composites after transient shear, Phys. Status Solidi B **244**, 4223 (2007).
[38] I. Alig, T. Skipa, D. Lellinger, and P. Pötschke, Destruction and formation of a carbon nanotube network in polymer melts: Rheology and conductivity spectroscopy, Polymer **49**, 3524 (2008).
[39] B. H. Cipriano, A. K. Kota, A. L. Gershon, C. J. Laskowski, T. Kashiwagi, H. A. Bruck, and S. R. Raghavan, Conductivity enhancement of carbon nanotube and nanofiber-based polymer nanocomposites by melt annealing, Polymer **49**, 4846 (2008).
[40] S. C. Schulz and W. Bauhofer, Shear influenced network dynamics and electrical conductivity recovery in carbon nanotube/epoxy suspensions, Polymer **51**, 5500 (2010).
[41] S. B. Kharchenko, J. F. Douglas, J. Obrzut, E. A. Grulke, and K. B. Migler, Flow-induced properties of nanotube-filled polymer materials, Nat. Mater. **3**, 564 (2004).
[42] H. Watanabe, Y. Matsumiya, M. Kakiuchi, and Y. Aoki, Rheo-dielectric behavior of carbon black suspensions, Nihon Reoroji Gakkaishi **29**, 77 (2001).
[43] L. Madec, M. Youssry, M. Cerbelaud, P. Soudan, D. Guyomard, and B. Lestriez, Surfactant for enhanced rheological, electrical, and electrochemical performance of suspensions for semisolid redox flow batteries and supercapacitors, ChemPlusChem **80**, 396 (2014).
[44] L. Madec, M. Youssry, M. Cerbelaud, P. Soudan, D. Guyomard, and B. Lestriez, Non-aqueous carbon black suspensions for lithium-based redox flow batteries: Rheology and simultaneous rheo-electrical behavior, Phys. Chem. Chem. Phys. **15**, 14476 (2013).
[45] M. Youssry, L. Madec, P. Soudan, M. Cerbelaud, D. Guyomard, and B. Lestriez, Formulation of flowable anolyte for redox flow batteries: Rheo-electrical study, J. Power Sources **274**, 424 (2015).
[46] T. Gibaud, D. Frelat, and S. Manneville, Heterogeneous yielding dynamics in a colloidal gel, Soft Matter **6**, 3482 (2010).
[47] V. Grenard, T. Divoux, N. Taberlet, and S. Manneville, Timescales in creep and yielding of attractive gels, Soft Matter **10**, 1555 (2014).
[48] Z. Liu, Y. Song, J. Zhou, and Q. Zheng, Simultaneous measurement of rheological and conductive properties of carbon black filled ethylene-tetrafluorothylene copolymer, J. Mater. Sci. **42**, 8757 (2007).
[49] F. Y. Fan, W. H. Woodford, Z. Li, N. Baram, K. C. Smith, A. Helal, G. H. McKinley, W. Craig Carter, and Y.-M. Chiang, Polysulfide flow batteries enabled by percolating nanoscale conductor networks, Nano Lett. **14**, 2210 (2014).
[50] M. Duduta, B. Ho, V. C. Wood, P. Limthongkul, V. E. Brunini, W. Craig Carter, and Y.-M. Chiang, Semi-solid lithium rechargeable flow battery, Adv. Energy Mater. **1**, 511 (2011).
[51] Z. Li, K. C Smith, Y. Dong, N. Baram, F. Y. Fan, J. Xie, P. Limthongkul, W. Craig Carter, and Y.-M. Chiang, Aqueous semi-solid flow cell: Demonstration and analysis, Phys. Chem. Chem. Phys. **15**, 15833 (2013).
[52] T.-S. Wei, F. Y. Fan, A. Helal, K. C. Smith, G. H. McKinley, Y.-M. Chiang, and J. A. Lewis, Biphasic electrode suspensions for Li-ion semi-solid flow cells with high energy density, fast charge transport, and low-dissipation flow, Adv. Energy Mater. **5**, 1500535 (2015).
[53] K. C. Smith, Y.-M. Chiang, and W. Craig Carter, Maximizing energetic efficiency in flow batteries utilizing non-Newtonian fluids, J. Electrochem. Soc. **161**, A486 (2014).
[54] A. Yoshimura and R. K. Prud'homme, Wall slip corrections for Couette disk viscometers and parallel, J. Rheol. **32**, 53 (1988).

[55] A. Gemant, The conception of a complex viscosity and its application to dielectrics, Trans. Faraday Soc. **31**, 1582 (1935).
[56] R. B. Bird and A. J. Giacomin, Who conceived the "complex viscosity"?, Rheol. Acta **51**, 481 (2012).
[57] A. Bard and L. Faulkner, *Electrochemical Methods: Fundamentals and Applications* (Wiley, New York, 2001).
[58] M. D. Dickey, R. C. Chiechi, R. J. Larsen, E. A. Weiss, D. A. Weitz, and G. M. Whitesides, Eutectic gallium-indium (EGaIn): A liquid metal alloy for the formation of stable structures in microchannels at room temperature, Adv. Funct. Mater. **18**, 1097 (2008).
[59] To achieve a higher torque resolution, by lowering the friction torque, one can top the liquid-metal bath with a layer of concentrated acid so as to limit the oxidation of gallium [Q. Xu, N. Oudalov, Q. Guo, H. M. Jaeger, and E. Brown, Effect of oxidation on the mechanical properties of liquid gallium and eutectic gallium-indium, Phys. Fluids **24**, 063101 (2012)]. Such a precaution was not necessary for the present study, but it could be used in future work.
[60] R. B. Bird, R. C. Armstrong, and O. Hassager, *Dynamics of Polymeric Liquids, Volume 1: Fluid Mechanics*, 2nd ed. (John Wiley & Sons, New York, 1987).
[61] J. B. Donnet, *Carbon Black: Science and Technology*, 2nd ed. (Taylor & Francis, London, 1993).
[62] K. M. Yearsley, M. R. Mackley, F. Chinesta, and A. Leygue, The rheology of multiwalled carbon nanotube and carbon black suspensions, J. Rheol. **56**, 1465 (2012).
[63] R. J. Samson, George W. Mulholland, and J. W. Gentry, Structural analysis of soot agglomerates, Langmuir **3**, 272 (1987).
[64] V. Trappe, E. Pitard, L. Ramos, A. Robert, H. Bissig, and L. Cipelletti, Investigation of q-dependent dynamical heterogeneity in a colloidal gel by x-ray photon correlation spectroscopy, Phys. Rev. E **76**, 051404 (2007).
[65] M. van der Waarden, Stabilization of carbon-black dispersions in hydrocarbons, J. Colloid Sci. **5**, 317 (1950).
[66] V. Trappe and D. A. Weitz, Scaling of the Viscoelasticity of Weakly Attractive Particles, Phys. Rev. Lett. **85**, 449 (2000).
[67] G. Ovarlez, L. Tocquer, F. Bertrand, and P. Coussot, Rheopexy and tunable yield stress of carbon black suspensions, Soft Matter **9**, 5540 (2013).
[68] J. Sprakel, S. B. Lindström, T. E. Kodger, and D. A. Weitz, Stress Enhancement in the Delayed Yielding of Colloidal Gels, Phys. Rev. Lett. **106**, 248303 (2011).
[69] N. Koumakis, E. Moghimi, R. Besseling, W. C. K. Poon, J. F. Brady, and G. Petekidis, Tuning colloidal gels by shear, Soft Matter **11**, 4640 (2015).
[70] Yacov Kantor and Itzhak Webman, Elastic Properties of Random Percolating Systems, Phys. Rev. Lett. **52**, 1891 (1984).
[71] M. M. Cross and A. Kaye, Simple procedures for obtaining viscosity/shear rate data from a parallel disc viscometer, Polymer **28**, 435 (1987).
[72] M. T. Shaw and Z. Z. Liu, Single-point determination of nonlinear rheological data from parallel-plate torsional flow, Applied Rheology **16**, 70 (2006).
[73] C. Clasen, Determining the true slip of a yield stress material with a sliding plate rheometer, Rheol. Acta **51**, 883 (2012).
[74] S. Zahirovic, A. S. Lubansky, Y. Leong Yeow, and D. V. Boger, Obtaining the steady shear rheological properties and apparent wall slip velocity data of a water-in-oil emulsion from gap-dependent parallel plate viscometry data, Rheol. Acta **48**, 221 (2009).
[75] C. O. Osuji and D. A. Weitz, Highly anisotropic vorticity aligned structures in a shear thickening attractive colloidal system, Soft Matter **4**, 1388 (2008).
[76] Note: here, the variable t denotes the critical exponent associated with the electrical percolation and not time.
[77] S. Kirkpatrick, Percolation and conduction, Rev. Mod. Phys. **45**, 574 (1973).
[78] J. P. Straley, Critical exponents for the conductivity of random resistor lattices, Phys. Rev. B **15**, 5733 (1977).
[79] J. P. Clerc, G. Giraud, J. M. Laugier, and J. M. Luck, The electrical conductivity of binary disordered systems, percolation clusters, fractals and related models, Adv. Phys. **39**, 191 (1990).
[80] I. Balberg, Tunneling and Nonuniversal Conductivity in Composite Materials, Phys. Rev. Lett. **59**, 1305 (1987).
[81] Z. Rubin, S. A. Sunshine, M. B. Heaney, I. Bloom, and I. Balberg, Critical behavior of the electrical transport properties in a tunneling-percolation system, Phys. Rev. B **59**, 12196 (1999).
[82] I. Balberg, A comprehensive picture of the electrical phenomena in carbon black-polymer composites, Carbon **40**, 139 (2002).
[83] T. Divoux, C. Barentin, and S. Manneville, From transient fluidization processes to Herschel-Bulkley behavior in simple yield stress fluids, Soft Matter **7**, 8409 (2011).
[84] T. Bauer, J. Oberdisse, and L. Ramos, Collective Rearrangement at the Onset of Flow of a Polycrystalline Hexagonal Columnar Phase, Phys. Rev. Lett. **97**, 258303 (2006).
[85] M. Siebenbürger, M. Ballauff, and T. Voigtmann, Creep in Colloidal Glasses, Phys. Rev. Lett. **108**, 255701 (2012).
[86] T. Brenner, S. Matsukawa, K. Nishinari, and R. Johannsson, Failure in a soft gel: Delayed failure and the dynamic yield stress, J. Non-Newtonian Fluid Mech. **196**, 1 (2013).
[87] M. Leocmach, C. Perge, T. Divoux, and S. Manneville, Creep and Fracture of a Protein Gel under Stress, Phys. Rev. Lett. **113**, 038303 (2014).
[88] J. Colombo and E. Del Gado, Stress localization, stiffening, and yielding in a model colloidal gel, J. Rheol. **58**, 1089 (2014).
[89] A. Kyrlidis, R. M. Sawka, G. D. Moeser, P. A. Kossyrev, and N. J. Hardman, High surface area and low structure carbon blacks for energy storage applications, U.S. Patent Application No. PCT/US2010/054,388 (5 May 2011).
[90] Sales specification: Vulcan XC72R, Cabot, 2008.
[91] Sales specification: Elftex 8, Cabot, 2008.
[92] Sales specification: Monarch 120, Cabot, 2003.
[93] M. Abramowitz and I. A. Stegun, *Handbook of Mathematical Functions* (Dover Publications, New York, 1972).